Temporal stability of multiple similarity solutions for porous channel flows with expanding or contracting walls

Sun, Yanxiao; Lin, Ping; Guo, Zhenlin

Published in:
Physics of Fluids

DOI:
10.1063/5.0051846

Publication date:
2021

Document Version
Peer reviewed version

Temporal stability of multiple similarity solutions for porous channel flows with expanding or contracting walls☆

Yanxiao Sun (孙燕晓)[1]

Beijing Key Laboratory for Magneto-Photoelectrical Composite and Interface Science, School of Mathematics and Physics, University of Science and Technology Beijing, Beijing 100083, China

Ping Lin[a,], Zhenlin Guo (郭震林)[b]*

[a]Department of Mathematics, University of Dundee, Dundee DD1 4HN, United Kingdom
[b]Mechanics Division, Beijing Computational Science Research Center, Building 9, East Zone, ZPark II, No. 10 East Xibeiwang Road, Haidian District, Beijing 100193, PR China

Abstract

In this paper, the temporal stability of multiple similarity solutions (flow patterns) for the incompressible laminar fluid flow along a uniformly porous channel with expanding or contracting walls is analyzed. This work extends the recent results of similarity perturbations of [1] by examining the temporal stability with perturbations of general form (including similarity and non-similarity forms). Based on the linear stability theory, two-dimensional eigenvalue problems associated with the flow equations are formulated and numerically solved by a finite difference method on staggered grids. The linear stability analysis reveals that the stability of the solutions is same with that under perturbations of a similarity form within the range of wall expansion ratio α ($-5 \leq \alpha \leq 3$ as in [1]). Further, it is found that the expansion ratio α has a great influence on the stability of type I flows: in the case of wall contraction ($\alpha < 0$), the stability region of the cross-flow Reynolds number (R) increases as the contraction ratio ($|\alpha|$) increases; in the case of wall expansion and $0 < \alpha \leq 1$, the stability region increases as the expansion ratio (α) increases; in the case of $1 \leq \alpha \leq 3$, type

*Corresponding author
Email address: p.lin@dundee.ac.uk (Ping Lin)

I flows are stable for all R where they exist. The flows of other types (types II and III with $-5 \leq \alpha \leq 3$ and type IV with $\alpha = 3$) are always unstable. As a nonlinear stability analysis or a validation of the linear stability analysis, the original nonlinear two-dimensional time dependent problem with an initial perturbation of general form over those flow patterns is solved directly. It is found that the stability with the non-linear analysis is consistent to the linear stability analysis.

Keywords: laminar flow, similarity solutions, expansion ratio, temporal stability, perturbations of general form

1. Introduction

The laminar flow in a porous channel with expanding or contracting walls has attracted much attention due to its wide applications in engineering and biomedicine, including transpiration cooling, phase sublimation, propellant burning, filtration, and blood transport in organisms. For example, the sublimation process of carbon dioxide, during which the walls expanded ([2]); propellant burning in a rocket motor with regressing walls ([3]); and fluid transport produced by expansion and contraction of a blood vessel ([4]).

The earliest investigations of steady flows across permeable and stationary walls can be traced back to Berman [5]. In his study, the laminar, two-dimensional flow of a viscous incompressible fluid in a porous channel with uniform injection (or suction) was considered. By assuming that the transverse velocity component was independent of the streamwise coordinate, the Navier-Stokes equations were reduced to a nonlinear ordinary differential equation with appropriate boundary conditions. Then Berman obtained an asymptotic expression for a small Reynolds number R by a perturbation method. A number of studies of porous channel flow followed. For example, Terrill [6] extended Berman's small R case and obtained series solutions for large R (for large suction), and Proudman [7] investigated the case of large R using an integral approach. Using the method of averages, Morduchow [8] obtained an analytical

solution for the entire injection range. Yuan [9] provided a perturbation solution for high injection case, and later, Terrill [10] modified the work of Yuan and provided a more accurate solution.

The earliest studies for moving walls can be traced back to Brady and Acrivos [11]. In their study, an exact solution to the Navier-Stokes equations for the flow in a channel with an accelerating surface velocity was presented. Along similar lines, Dauenhauer and Majdalani [2] obtained a self-similar solution for a porous channel flow with expanding or contracting walls. They assumed that the wall expansion ratio α was a constant and reduced the Navier-Stokes equations to a boundary value problem of a fourth-order nonlinear ordinary differential equation that could be solved by a shooting method. In a later study, asymptotic solutions for this problem were presented by Majdalani *et al.* [4] for small R and by Majdalani and Zhou [12] for moderate-to-large R. Zhou and Majdalani [3] also provided an analytical solution for slab rocket motors with regressing walls. Recently, Xu *et al.* [13] investigated multiple solutions of the case for which the wall expansion ratio α may be varied from α_0 to α_1 through some given functions, and concluded that the solutions quickly reached the steady state. More recently, Majdalani and Xuan [14] improved the results in [12] and obtained a complete asymptotic solution for the problem of channel flow with moving walls. In their work, a viscous boundary layer correction was provided to overcome the singular pressure distribution and its normal gradients near the midsection plane of the expanding porous channel. Later, a wavelet-homotopy method was developed by Chen and Xu [15] to give solutions to this problem. For a porous tube with an expanding or contracting sidewall, analytical solutions for both large and small Reynolds number with small-to-moderate α were obtained by Saad and Majdalani [16] recently.

As for the stability of the solutions, Durlofsky and Brady [17] investigated the spatial stability of the solutions for two-dimensional porous wall channel and accelerating-wall channel flows under linear symmetric perturbations. For the same porous wall problem, Ferro and Gnavi [18] extended the results of Durlofsky and Brady to symmetric and asymmetric solutions, and analyzed the

spatial stability of small perturbations of arbitrary shape. The temporal stability of these flows was examined by Zaturska *et al.* [19]. They proved that most of these flows were temporally unstable to two-dimensional antisymmetric perturbations. Later, Taylor *et al.* [20] generalized the work of Zaturska to three-dimensional flows. Watson *et al.* [21] investigated the temporal stability of asymmetric flows arising from a channel with porous and accelerating walls. For porous channel flows with expanding or contracting walls, the temporal stability analysis was presented in [1]. It is noted that all the perturbations used in the above temporal stability analysis are constrained to the form of the similarity transformation. We would also like to mention a few other recent work on linear stability analysis of relevant channel or duct flow problems. For flows in solid rocket motors, the stability was investigated in [22, 23, 24]. The temporal stability analysis of pressure-driven flows in channels patterned with superhydrophobic surfaces containing periodic grooves and ribs aligned longitudinally to the flow direction was performed by Yu *et al.* [25], and the stability of a pressure driven flow in a duct heated from below and subjected to a vertical magnetic field was studied by Qi *et al.* [26].

From both physical and mathematical points of view, the perturbation of a flow solution (no matter whether it is a similarity solution or not) is not necessarily in the similarity form. So to study the stability properly and accurately we have to consider the perturbation in a general form (including similarity and non-similarity forms). This is the purpose of this paper, that is, to investigate the temporal stability of similarity solutions (for flows in a channel with expanding or contracting walls) under perturbations of general form. The basic equations of the problem and the multiple solutions are described in Section 2. The linear stability analysis of these solutions by numerical means is carried out in Section 3. The linear stability theory is based on linear approximation of the nonlinear equations, which does not cover the nonlinear temporal development of an initial perturbation. So in Section 4 a non-linear analysis is conducted by directly solving the nonlinear Navier-Stokes equations with small-amplitude initial perturbations of general form. Section 5 is devoted to the conclusions.

2. Mathematical formulation of the flow problem

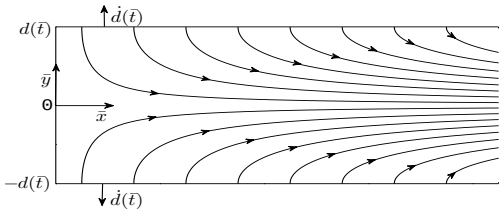

Figure 1: Diagram of the two-dimensional channel with expanding or contracting porous walls. The plotted streamlines correspond to a symmetric steady flow pattern.

Consider the two-dimensional, laminar and incompressible flow in a rectangular channel with two permeable and moving walls. As shown in Fig. 1, which depicts the cross section of the simulated domain. The channel height is $2d$ and the channel length is semi-infinite. Both sidewalls have the same permeability and expand or contract uniformly at a time-dependent rate $\dot{d}$, where $\dot{}$ means the derivation of $\bar{t}$. Additionally, with $\bar{x}$ representing the streamwise direction and $\bar{y}$ the normal direction, the corresponding streamwise and normal velocity components are defined as $\bar{u}$ and $\bar{v}$, respectively. The over-bar is used to denote dimensional variables. Under these assumptions, let the velocity vector $\bar{\mathbf{v}} = (\bar{u}, \bar{v})$, the general continuity and motion equations are given as

$$\nabla \cdot \bar{\mathbf{v}} = 0, \tag{1}$$

$$\frac{\partial \bar{\mathbf{v}}}{\partial \bar{t}} + \bar{\mathbf{v}} \cdot \nabla \bar{\mathbf{v}} = -\frac{1}{\rho} \nabla \bar{p} + \nu \triangle \bar{\mathbf{v}}, \tag{2}$$

where ∇ is the gradient operator and $\triangle$ is the Laplace operator, $\bar{p}$, ρ, $\bar{t}$ and ν are the dimensional pressure, density, time and kinematic viscosity, respectively. The boundary conditions are

$$\bar{u}|_{\bar{y}=d} = 0, \quad \bar{v}|_{\bar{y}=d} = -v_w = -A\dot{d}, \tag{3}$$

$$\bar{u}|_{\bar{y}=-d} = 0, \quad \bar{v}|_{\bar{y}=-d} = v_w, \tag{4}$$

$$\bar{u}|_{\bar{x}=0} = 0, \tag{5}$$

where v_w is the injection velocity at the wall, which is assumed to be independent of position. $A = v_w/\dot{d}$ is a constant which is a measure of the wall permeability. The condition (5) can be achieved by making the flow symmetrical with respect to the plane $\bar{x} = 0$, where $\bar{v}$ is left free.

Next, we introduce the following scalings:

$$u = \frac{\bar{u}}{v_w}, \quad v = \frac{\bar{v}}{v_w}, \quad x = \frac{\bar{x}}{d}, \quad y = \frac{\bar{y}}{d}, \quad t = \frac{v_w \bar{t}}{d}, \quad p = \frac{\bar{p}}{\rho v_w^2}, \tag{6}$$

then the following dimensionless equations are obtained.

$$\nabla \cdot \mathbf{v} = 0, \tag{7}$$

$$(1 - \frac{2\alpha t}{R})\frac{\partial \mathbf{v}}{\partial t} - (\frac{\alpha}{R}x)\frac{\partial \mathbf{v}}{\partial x} - (\frac{\alpha}{R}y)\frac{\partial \mathbf{v}}{\partial y} - \frac{\alpha}{R}\mathbf{v} + \mathbf{v} \cdot \nabla \mathbf{v} = -\nabla p + \frac{1}{R}\triangle \mathbf{v}. \tag{8}$$

The original boundary conditions become

$$u|_{y=1} = 0, \quad v|_{y=1} = -1, \tag{9}$$

$$u|_{y=-1} = 0, \quad v|_{y=-1} = 1, \tag{10}$$

$$u|_{x=0} = 0. \tag{11}$$

Here, $\mathbf{v} = (u, v)$ and

$$\alpha = \frac{\dot{d}d}{\nu} \tag{12}$$

is the wall expansion ratio. $\alpha > 0$ implies the expansion and $\alpha < 0$ the contraction. R is the cross-flow Reynolds number defined by $R = dv_w/\nu$. We can infer that $R > 0$ is for the injection and $R < 0$ for the suction. In the current study, we just consider the case for which R is time invariant. It follows that α is constant and can be specified by its initial value $\dot{d}_0 d_0/\nu$, where d_0 and $\dot{d}_0$ are the initial channel half-height and expansion rate, respectively. Integrating (12), the channel height of the present solution will vary in time according to $d = \sqrt{d_0^2 + 2\nu\alpha\bar{t}}$.

The dimensionless flow problem admits an exact similarity solution of the form

$$\mathbf{v} = (xf_y(y,t), -f(y,t)). \tag{13}$$

For flows symmetric with respect to the midsection plane ($\bar{y} = 0$), the velocity satisfies the boundary conditions (3) and

$$\frac{\partial \bar{u}}{\partial \bar{y}}|_{\bar{y}=0} = 0, \quad \bar{v}|_{\bar{y}=0} = 0, \tag{14}$$

which are the same as (3) and (4) in [1], respectively. Further, the dimensionless boundary conditions become (9) and

$$\frac{\partial u}{\partial y}|_{y=0} = 0, \quad v|_{y=0} = 0. \tag{15}$$

By using (13) into (7) and (8) , we obtain a differential equation for the similarity function f,

$$(1 - \frac{2\alpha t}{R}) f_{yyt} - \frac{1}{R} f_{yyyy} - f f_{yyy} + f_y f_{yy} - \frac{\alpha}{R}(y f_{yyy} + 3 f_{yy}) = 0, \tag{16}$$

the boundary conditions are

$$f(0) = 0, \quad f(1) = 1, \quad f_y(1) = 0, \quad f_{yy}(0) = 0. \tag{17}$$

In particular, there are symmetric steady solutions with

$$\mathbf{U} = (xF_y, -F), \tag{18}$$

where

$$F'''' + R(FF''' - F'F'') + \alpha(yF''' + 3F'') = 0, \tag{19}$$

and

$$F(0) = 0, \quad F(1) = 1, \quad F'(1) = 0, \quad F''(0) = 0. \tag{20}$$

Here, a prime denotes differentiation with respect to y. Particularly, equation (19) is Berman's classic equation in [5] when $\alpha = 0$.

Remark 1. *Some researchers also consider the asymmetric solutions satisfying the boundary conditions*

$$F(-1) = -1, \quad F(1) = 1, \quad F'(-1) = 0, \quad F'(1) = 0. \tag{21}$$

In this paper we shall mainly consider stability of symmetric steady solutions which satisfy the boundary conditions (20).

The numerical solutions of (19) and (20) at some selected values of α ($\alpha = 0$, $\pm 1/2$, ± 1, ± 2, ± 3 and -5) have been investigated in [1]. Here we need to consider these solutions again for the analysis of their stability and they are shown in Figs. 2 and 3, which are from [1]. It can be seen that for a fixed value of α ($-5 \leq \alpha \leq 3$), the typical state variable $-F''(1)$ is plotted as a function of R. (The quantity $-F''(1)$ is proportional to the skin friction at the upper wall.) As described in [1], there are multiple solutions. In each case of $-5 \leq \alpha \leq 2$, three different types of solutions are found, which are classified as being of types I, II and III: type I is in $-\infty < R < \infty$, types II and III exist in a common semi-infinite domain, spanning over $-\infty < R < R_\alpha$. Where R_α is the common point of types II and III for the corresponding α, and $R_{-5} = -14.486$, $R_{-3} = -13.918$, $R_{-2} = -13.482$, $R_{-1} = -12.909$, $R_{-1/2} = -12.561$, $R_0 = -12.165$, $R_{1/2} = -11.724$, $R_1 = -11.245$ and $R_2 = -10.295$. When $\alpha = 3$, a new type of solutions is found, which is marked as IV. While other types of solutions, similar to the classification for $-5 \leq \alpha \leq 2$, are marked as I, II and III: type I is in $R_3^1 < R < \infty$ and type IV is in $R_3^1 < R < -0.796$, types II and III exist in a common semi-infinite domain $-\infty < R < R_3^2$. Where $R_3^1 = -4.25$ and $R_3^2 = -9.545$ are the common points for types I, IV and types II, III, respectively. These results are presented in Table 1. Note that ∞ and $-\infty$ in this paper stand for relatively large or negatively large values, respectively.

Remark 2. *We can also present the bifurcation diagram as a function of α. For example, Fig. 4 shows bifurcation diagrams for a couple of R values. For $R = -14$ (see Fig. 4(a)), there is just one symmetric solution (type I solution) for $-5 \leq \alpha < -3.225$, and there are three symmetric solutions (types I, II and III solutions) for $-3.225 < \alpha \leq 2$. The common point of types II and III is $\alpha = -3.225$. For $R = -30$ (see Fig. 4(b)), there are three types (types I, II and III) solutions for $-5 \leq \alpha \leq 2$. In this paper we consider the stability of steady solutions for a range of values of α, so we will not explore this type of bifurcation diagrams further.*

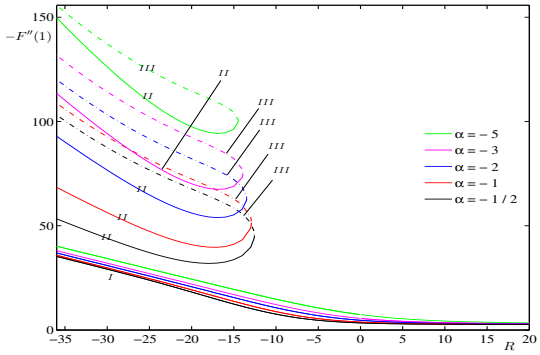

Figure 2: Values of $-F''(1)$ versus R for the types I, II and III symmetric solutions. To make it easier to distinguish, the solutions of types II and III at the same α are drawn with solid and chain lines of the same color, respectively. Reproduced from the manuscript version available in "https://discovery.dundee.ac.uk/ws/portalfiles/portal/37693294/final_manuscript.pdf"; licensed under a Creative Commons Attribution (CC BY) license.

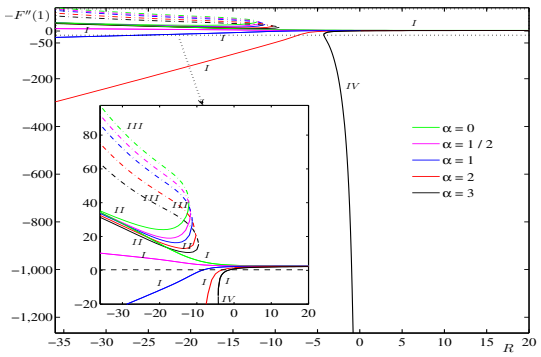

Figure 3: Values of $-F''(1)$ versus R for the types I, II, III and IV symmetric solutions. To make it easier to distinguish, similarly, the solutions of types II and III at the same α are drawn with solid and chain lines of the same color, respectively. Reproduced from the manuscript version available in "https://discovery.dundee.ac.uk/ws/portalfiles/portal/37693294/final_manuscript.pdf"; licensed under a Creative Commons Attribution (CC BY) license.

Table 1: Summary of multiple solutions for porous channel flows with various values of α ($-5 \leq \alpha \leq 3$).

α	number of solutions found	type designation	existence ranges
-5	3	I	$(-\infty,\infty)$
		II, III	$(-\infty,R_{-5})$
-3	3	I	$(-\infty,\infty)$
		II, III	$(-\infty,R_{-3})$
-2	3	I	$(-\infty,\infty)$
		II, III	$(-\infty,R_{-2})$
-1	3	I	$(-\infty,\infty)$
		II, III	$(-\infty,R_{-1})$
$-1/2$	3	I	$(-\infty,\infty)$
		II, III	$(-\infty,R_{-1/2})$
0	3	I	$(-\infty,\infty)$
		II, III	$(-\infty,R_0)$
$1/2$	3	I	$(-\infty,\infty)$
		II, III	$(-\infty,R_{1/2})$
1	3	I	$(-\infty,\infty)$
		II, III	$(-\infty,R_1)$
2	3	I	$(-\infty,\infty)$
		II, III	$(-\infty,R_2)$
3	4	I	(R_3^1,∞)
		II, III	$(-\infty,R_3^2)$
		IV	$(R_3^1,-0.796)$

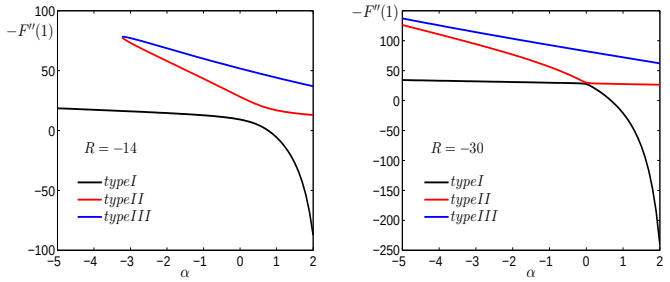

(a) $R = -14$ (b) $R = -30$

Figure 4: Values of $-F''(1)$ versus α for the types I, II and III symmetric solutions. The cross-flow Reynolds numbers are (a) $R = -14$ and (b) $R = -30$.

As described in [1], the characteristics of the four types of flows represented by the solutions are as follows:

(1) Type I covers the flows whose axial velocity profiles have a maximum at the center of the channel.

(2) Type II includes the flows whose axial velocity profiles have an inflection point and a maximum between the center of the channel and the wall and whose centerline velocity is positive for negative R far away from 0.

(3) Type III contains axial velocity profiles with the same form as type II but with reverse flow at the center of the channel.

(4) Type IV includes the flows which have reverse flow near the wall of the channel, and the wall velocity gradient ($F''(1)$) for these flows increases rapidly with the increase of R.

The axial velocity profiles $F'(y)$ for type I solutions with some injection and suction cross-flow Reynolds numbers over a range of wall expansion ratios are described in Figs. 5 and 6. In each case of R, increasing wall expansion ratio increases the axial velocity near the center of the channel and decreases near the wall. This behaviour is reversed for the case of contracting channel. In addition, the profiles for each case of α have a maximum at the center of the channel.

For $R > 0$ (injection), they monotonically decrease to 0 at the wall, and the velocity at the centerline ($F'(0)$) is approximately equal to 1.57 as $R \to \infty$. For $R < 0$ (suction), when the expansion ratio $-5 \leq \alpha \leq 1/2$, the profiles are still monotonic functions of y. Further, for negative R far away from 0, the profiles for $\alpha \leq 0$ are approximately equal to 1 everywhere except in a thin boundary layer forming above the wall, while the profiles for $\alpha = 1/2$ have a centerline velocity approximately equal to 1.4317. When $\alpha \geq 1$, the profiles are no longer monotonic below a negative value of R which depends on the value of α. Instead, they pass through a minimum (which is negative) before going to 0 at the wall, this can be seen from Fig. 6(b), which indicates reverse flow occurs near the wall.

The axial velocity profiles for type II solutions are described in Fig. 7. For each case of α, it can be observed in Fig. 7(a) that the profiles have a minimum at the centerline and then pass through a maximum before going to zero at the wall. Further, for negative R far away from 0, the velocity for $\alpha \geq 0$ is close to 1 everywhere except in a boundary layer (see Fig. 7(b)), which is similar to that described for type I solutions with $\alpha \leq 0$. The axial velocity profiles for type III solutions are depicted in Fig. 8. For each case of α, these profiles have the same shape as those of type II, except that there is a region of reverse flow near the center of the channel at any R where these solutions exist.

Fig. 9 illustrates the velocity profiles for four types of solutions at $\alpha = 3$. For types I, II and III solutions, the profiles (shown in Fig. 9(a)) have similar characteristics with those for types I, II and III solutions at $\alpha = 2$, respectively. For type IV solutions, the profiles (shown in Fig. 9(b)) are characterized by a rapid increase in the centerline velocity and the wall velocity gradient ($F''(1)$) as R increases, and the development of reverse flow near the wall of the channel.

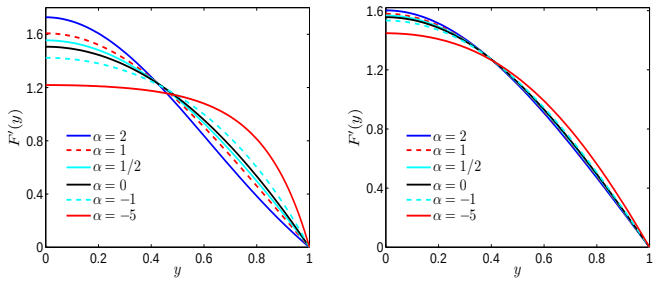

(a) $R = 1$ (b) $R = 30$

Figure 5: Axial velocity profiles $F'(y)$ for type I solutions over a range of wall expansion ratios α and an injection cross-flow Reynolds number of (a) $R = 1$ and (b) $R = 30$.

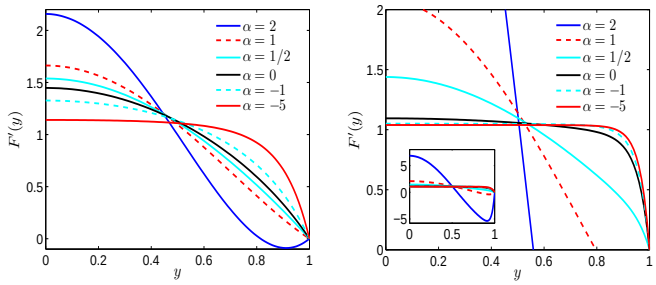

(a) $R = -5$ (b) $R = -25$

Figure 6: Axial velocity profiles $F'(y)$ for type I solutions over a range of wall expansion ratios α and a suction cross-flow Reynolds number of (a) $R = -5$ and (b) $R = -25$.

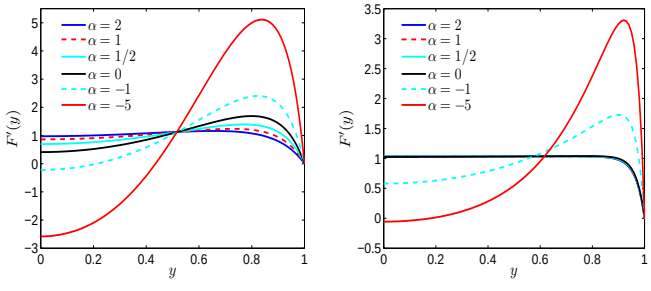

(a) $R = -14.5$ (b) $R = -35$

Figure 7: Axial velocity profiles $F'(y)$ for type II solutions over a range of wall expansion ratios α and a suction cross-flow Reynolds number of (a) $R = -14.5$ and (b) $R = -35$.

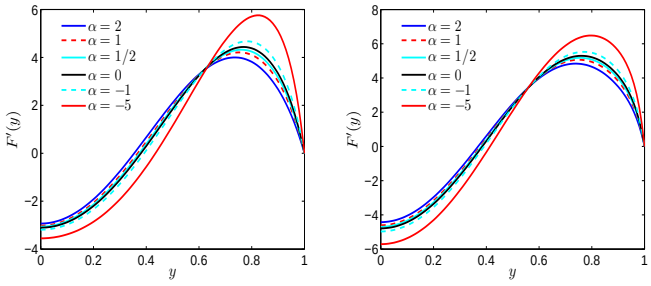

(a) $R = -15$ (b) $R = -35$

Figure 8: Axial velocity profiles $F'(y)$ for type III solutions over a range of wall expansion ratios α and a suction cross-flow Reynolds number of (a) $R = -15$ and (b) $R = -35$.

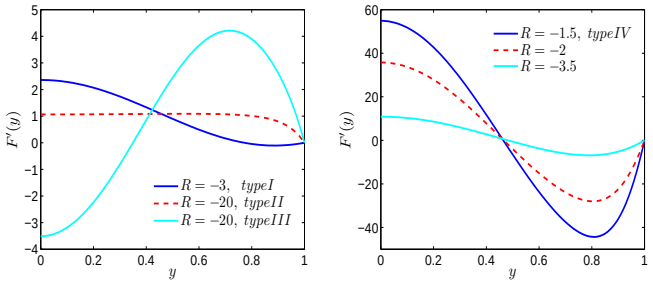

(a) (b)

Figure 9: Axial velocity profiles $F'(y)$ for solutions of (a) types I, II and III and (b) type IV over some values of R; $\alpha = 3$.

The temporal stability analysis of above steady flows (denoted as $\mathbf{U}$) under perturbations of the similarity form (13) is given in [1]. Although the similarity solutions are considered, from both physical and mathematical points of view, the perturbations are not necessarily of the similarity form. So it is not complete to examine the stability of the flows only for the perturbations of the similarity form. In this paper we investigate the temporal stability with perturbations of general form (including similarity and non-similarity forms). We shall adopt the numerical means later, and for numerical study, we can only deal with finite domain. We truncate the infinite domain to an artificial boundary at $x = x_r$, and develop and impose a proper boundary condition at $x = x_r$ in order for the resulted steady solutions to be consistent with the similarity solutions and facilitate comparison with previous analysis in [1]. The conditions read:

$$u|_{y=1} = 0, \quad v|_{y=1} = -1, \tag{22}$$

$$u|_{y=-1} = 0, \quad v|_{y=-1} = 1, \tag{23}$$

$$u|_{x=0} = 0, \quad \frac{\partial v}{\partial x}|_{x=0} = 0, \tag{24}$$

$$u - x\frac{\partial u}{\partial x}|_{x=x_r} = 0, \quad \frac{\partial v}{\partial x}|_{x=x_r} = 0. \tag{25}$$

It is not difficult to verify that all steady state similarity solutions satisfy the proposed condition (25) at the artificial boundary.

3. Temporal stability analysis

Here we examine the linear temporal stability of above steady flows under perturbations of general form (including similarity and non-similarity forms), in order to determine whether such perturbations could destabilize a flow which is stable under perturbations of the similarity form (13). We write the perturbed velocity and pressure fields

$$\mathbf{v} = \mathbf{U} + \mathbf{v_1} = (xF_y, -F) + (u_1, v_1), \quad p = P + p_1, \tag{26}$$

where P is the unperturbed pressure, $\mathbf{v_1}$ and p_1 are infinitesimal perturbations for the steady flow $\mathbf{U}$ and P, respectively. Substituting (26) into the dimensionless equations (7), (8) and boundary conditions (22)-(25), and linearizing (8) for $\mathbf{v_1}$, we obtain the following linearized perturbation equations

$$\nabla \cdot \mathbf{v_1} = 0, \tag{27}$$

$$(1 - \frac{2\alpha t}{R})\frac{\partial \mathbf{v_1}}{\partial t} - (\frac{\alpha}{R}x)\frac{\partial \mathbf{v_1}}{\partial x} - (\frac{\alpha}{R}y)\frac{\partial \mathbf{v_1}}{\partial y} - \frac{\alpha}{R}\mathbf{v_1} + (\mathbf{v_1} \cdot \nabla)\mathbf{U} + (\mathbf{U} \cdot \nabla)\mathbf{v_1} = -\nabla p_1 + \frac{1}{R}\triangle \mathbf{v_1}, \tag{28}$$

and boundary conditions

$$u_1|_{y=1} = 0, \quad v_1|_{y=1} = 0, \tag{29}$$

$$u_1|_{y=-1} = 0, \quad v_1|_{y=-1} = 0, \tag{30}$$

$$u_1|_{x=0} = 0, \quad \frac{\partial v_1}{\partial x}|_{x=0} = 0, \tag{31}$$

$$u_1 - x\frac{\partial u_1}{\partial x}|_{x=x_r} = 0, \quad \frac{\partial v_1}{\partial x}|_{x=x_r} = 0. \tag{32}$$

The perturbations ($\mathbf{v_1}$) are of general form and include those of the similarity form (13) considered in [1].

Based on the method of separation of variables, the perturbations $\mathbf{v_1}$ and

p_1 can be expressed in the following forms

$$\begin{cases} u_1 = \hat{u}(x,y)e^{st}, \quad v_1 = \hat{v}(x,y)e^{st}, \quad p_1 = \hat{p}(x,y)e^{st}, \quad (\alpha = 0) \\ u_1 = \hat{u}(x,y)e^{-st_1}, \quad v_1 = \hat{v}(x,y)e^{-st_1}, \quad p_1 = \hat{p}(x,y)e^{-st_1}, \quad (\alpha < 0) \\ u_1 = \hat{u}(x,y)e^{-st_2}, \quad v_1 = \hat{v}(x,y)e^{-st_2}, \quad p_1 = \hat{p}(x,y)e^{-st_2}, \quad (\alpha > 0) \end{cases} \tag{33}$$

where

$$\begin{cases} t_1 = \ln(1 - \dfrac{2\alpha t}{R}), \quad (\alpha < 0) \\ t_2 = -\ln(1 - \dfrac{2\alpha t}{R}). \quad (\alpha > 0) \end{cases} \tag{34}$$

By using the dimensionless transformation $t = v_w\bar{t}/d = R\nu\bar{t}/d^2 = R\nu\bar{t}/(d_0^2 + 2\nu\alpha\bar{t})$ into (34), we obtain

$$\begin{cases} t_1 = \ln(\dfrac{d_0^2}{d^2}), \quad (\alpha < 0) \\ t_2 = -\ln(\dfrac{d_0^2}{d^2}). \quad (\alpha > 0) \end{cases} \tag{35}$$

In (33), $\hat{u}(x,y)$, $\hat{v}(x,y)$ and $\hat{p}(x,y)$ are the amplitudes of the corresponding perturbations, s is the complex eigenvalue. The real part of s ($Re(s)$) represents the growth or decay rate of the perturbation. When $\alpha = 0$, $Re(s)$ represents the growth rate for $R > 0$, while for $R < 0$, the sign of t becomes negative and $Re(s)$ represents the decay rate. When $\alpha < 0$ (for contraction), t_1 is positive and $Re(s)$ is the decay rate. When $\alpha > 0$ (for expansion), we note that t is finite, and when $t \to (R/2\alpha)$, the channel height d has already reached infinity. Hence, t_2 is also positive and $Re(s)$ is the decay rate. That is, for $\alpha = 0$ and $R > 0$, eigenvalues with positive real parts ($Re(s)$) indicate growing perturbations, so the instability is implied if there is an eigenvalue such that $Re(s) > 0$; while for the case of $\alpha \neq 0$ and the case of $\alpha = 0$ and $R < 0$, eigenvalues with negative real parts indicate growing perturbations, so the instability is implied if there is an eigenvalue such that $Re(s) < 0$. Especially when $\alpha > 0$ (for expansion), the instability occurs at $t \to (R/2\alpha)$. The imaginary part of s ($Im(s)$) represents the dimensionless frequency of the corresponding perturbation. If s is real, the perturbations either grow or decay monotonically.

Substituting (33) into (27) and (28), we have the following eigenvalue problems:

$$\begin{cases} -(\hat{u}_{xx}+\hat{u}_{yy})+R(F_y\hat{u}+xF_{yy}\hat{v})+R(xF_y\hat{u}_x-F\hat{u}_y)+R\hat{p}_x \\ =-Rs\hat{u}, \\ -(\hat{v}_{xx}+\hat{v}_{yy})+R(-F_y\hat{v})+R(xF_y\hat{v}_x-F\hat{v}_y)+R\hat{p}_y \\ =-Rs\hat{v}, \\ \hat{u}_x+\hat{v}_y=0, \qquad (\alpha=0) \end{cases} \tag{36}$$

$$\begin{cases} -(\hat{u}_{xx}+\hat{u}_{yy})-(\alpha x)\hat{u}_x-(\alpha y)\hat{u}_y-\alpha\hat{u}+R(F_y\hat{u}+xF_{yy}\hat{v})+R(xF_y\hat{u}_x-F\hat{u}_y)+R\hat{p}_x \\ =2G\alpha s\hat{u}, \\ -(\hat{v}_{xx}+\hat{v}_{yy})-(\alpha x)\hat{v}_x-(\alpha y)\hat{v}_y-\alpha\hat{v}+R(-F_y\hat{v})+R(xF_y\hat{v}_x-F\hat{v}_y)+R\hat{p}_y \\ =2G\alpha s\hat{v}, \\ \hat{u}_x+\hat{v}_y=0, \qquad (\alpha\neq 0) \end{cases} \tag{37}$$

where $G=-1$ for $\alpha<0$ and $G=+1$ for $\alpha>0$, all associated with the boundary conditions

$$\begin{cases} \hat{u}|_{y=1}=0, \quad \hat{v}|_{y=1}=0, \\ \hat{u}|_{y=-1}=0, \quad \hat{v}|_{y=-1}=0, \\ \hat{u}|_{x=0}=0, \quad \dfrac{\partial\hat{v}}{\partial x}|_{x=0}=0, \\ \hat{u}-x\dfrac{\partial\hat{u}}{\partial x}|_{x=x_r}=0, \quad \dfrac{\partial\hat{v}}{\partial x}|_{x=x_r}=0. \end{cases} \tag{38}$$

To overcome the difficulty of lacking a boundary condition for the pressure, the discretization of the eigenvalue problem (37) (for $\alpha>0$) associated with (38) is done on the staggered grid (Fig. 20) introduced by Harlow and Welch [27] . The corresponding finite difference scheme is given in Appendix A. Similar finite difference schemes have been constructed for eigenvalue problems associated with other α.

The eigenvalue pencil of the real unsymmetric eigenvalue problem (A3) satisfying (A4) contains real values and complex conjugate pairs. To detect the flow instability, we need to seek the eigenvalues with the maximal or minimal

real part that corresponds to the least stable eigenvalues. For the case of $\alpha \neq 0$ and the case of $\alpha = 0$ and $R < 0$, the least stable eigenvalues are those with the minimal real part (i.e., the minimum decay rate). For $\alpha = 0$ and $R > 0$, the opposite is true, and the least stable eigenvalues are those with the maximal real part (i.e., the maximum growth rate).

We also need to determine a proper artificial boundary (the truncated channel length) $x = x_r$ for the eigenvalue computation. It should not be too large in order to save the computational time. In the meanwhile it should not affect the stability study. Fig. 10 shows the minimal real part of the eigenvalues (marked by q) versus R for $\alpha = 1/2$ with $x_r = 5$, 10 and 20 and with a 10×800 mesh. The figure suggests that the stability of the three types (types I, II and III) solutions behaves the same for the three choices of artificial channel lengths. We thus choose a smaller $x_r = 5$ in all the following computations so as to reduce the overall computational cost.

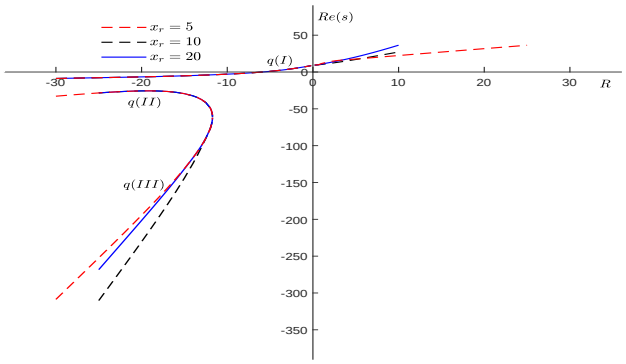

Figure 10: Real part (q) of the least stable eigenvalues for types I, II and III solutions with $\alpha = 1/2$.

We now numerically study the stability of symmetric steady solutions with the wall expansion ratio $-5 \leq \alpha \leq 3$ under the above mentioned parameter setting. A uniform mesh (10×800) is used in our calculation of eigenvalues.

The real part of the least stable eigenvalues for (36) and (37) is plotted versus R in Figs. 11-13. We mark the minimal real part of the eigenvalues as q in the case of $\alpha \neq 0$. When $\alpha = 0$, q represents the maximal real part for $R > 0$ and the minimum real part for $R < 0$.

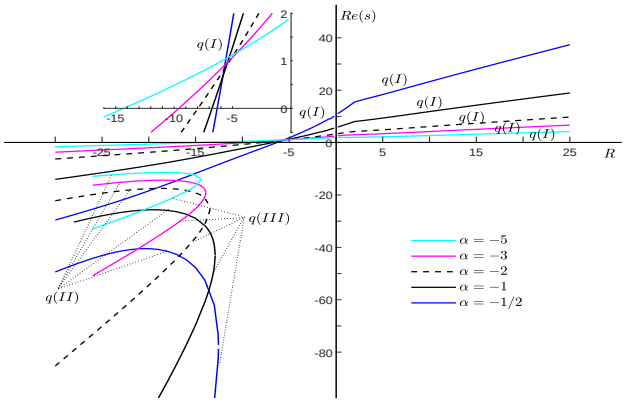

Figure 11: Real part (q) of the least stable eigenvalues for types I, II and III solutions with various values of α ($-5 \leq \alpha \leq -1/2$) under perturbations of general form.

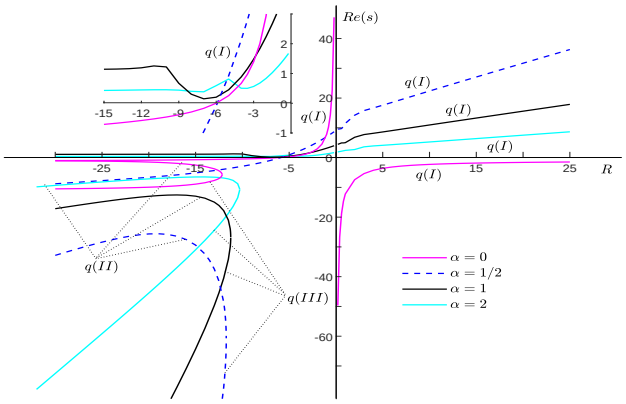

Figure 12: Real part (q) of the least stable eigenvalues for types I, II and III solutions with various values of α ($0 \le \alpha \le 2$) under perturbations of general form.

Table 2: Comparison of the least stable eigenvalues for type I solutions with $\alpha = 2$ and various R ($10 \le R \le 50$).

R	s of this paper	s of [1]
10	$5.25217952 + 15.23227764i$	11.83190084
20	$7.53177378 + 33.96909925i$	27.36806892
30	$9.80930566 + 52.75361865i$	43.55348327
40	$12.08494339 + 71.5616992i$	59.49375546
50	$14.36096663 + 90.38412325i$	75.33930753

Table 3: The stability ranges of R of type I solutions with various values of α ($-5 \le \alpha \le 2$) under perturbations of general form.

α	stability ranges of R	α	stability ranges of R	α	stability ranges of R
-5	(-14.315,∞)	-1	(-6.759,∞)	1/2	(-5.905,∞)
-3	(-9.605,∞)	-1/2	(-6.317,∞)	1	($-\infty$,∞)
-2	(-7.961,∞)	0	(-6.001,∞)	2	($-\infty$,∞)

For type I solutions with $-5 \le \alpha \le 2$, when $R > 0$, we note that the real

part of each of the eigenvalues is positive for $\alpha \neq 0$, and negative for $\alpha = 0$, namely no amplification of perturbations occurs and the injection flows are always stable. In addition, we note that except for a small range of $R > 0$, the least stable eigenvalues are not the same as that in the case of perturbations in similarity form (13), while the stability range is the same. As an example, for type I solutions with $\alpha = 2$ and $10 \leq R \leq 50$, the comparison of eigenvalues with the minimum decay rate is shown in Table 2. For each case of R, the decay rate of the present least stable perturbation is smaller than that of the least stable perturbation of [1], implying that the present perturbation decays more slowly. When $R < 0$ (that is, when there is suction), the stability of type I solutions varies for different α. For each case of $-5 \leq \alpha \leq 1/2$, as R decreases, the branch $q(I)$ representing the minimum decay rate crosses the line $Re(s) = 0$ at a particular value of R, which corresponds to the critical cross-flow Reynolds number. Then the value of q becomes negative below this critical cross-flow Reynolds number, which indicates that the perturbations are expected to grow in time and the suction flows become unstable. For each case of $1 \leq \alpha \leq 2$, the minimum decay rate for type I solutions is positive for $R < 0$ and hence these type I flows are always stable in this region. The critical cross-flow Reynolds numbers and the stability ranges of R of type I solutions with $\alpha = i$ ($i = 0$, $\pm 1/2$, ± 1, ± 2, -3 and -5) are shown in Table 3, which are consistent with those in [1]. For $\alpha < 0$ (in the case of wall contraction), we find that the critical cross-flow Reynolds number decreases and the stability region increases as the contraction ratio ($|\alpha|$) increases; for $\alpha > 0$ (in the case of wall expansion), the critical R decreases and the stability region increases as the expansion ratio (α) increases. One possible explanation for this behaviour is as follows: in the case of wall contraction ($\alpha < 0$), for larger contraction ratio ($|\alpha|$), the channel half-height d decreases faster. Combining (33) and (35), for the same least stable eigenvalue s with positive real part, the perturbation with the larger contraction ratio will decay more rapidly. When $\alpha > 0$, for larger expansion ratio (α), the channel half-height d increases faster. Then for the same least stable eigenvalue s with positive real part, the perturbation with the larger expansion ratio will

decay more rapidly. We further note that, when α is larger, i.e., $\alpha \geq 1$, and $R < 0$, an inflection point (at which the acceleration changes from decrease to increase) appears in the axial velocity profiles near the wall. We observe that as R decreases to some point the flow reversal occurs near the wall since the rapid volumetric expansion of the wall causes a sudden mass deficiency near the closed head end. The incompressible fluid is thus forced to flow upstream along the head end to occupy the space accompanying the expansion process. Then the same fluid has to turn later and head downstream towards the suction sites along the porous surface ([2]). This can be seen in Fig. 6 where the axial velocity profiles of type I solutions are illustrated. In comparison with the stability results of type I solutions with $\alpha = 1/2$, where the axial velocity profiles have no inflection points, it seems that the presence of an inflection point (or the flow acceleration changes from decrease to increase) near the wall may stabilize the flow.

For types II and III solutions with $-5 \leq \alpha \leq 2$, the minimum decay rate (q) remains negative for $-\infty < R < R_i$ in the case of $\alpha = i$ ($i = 0$, $\pm 1/2$, ± 1, ± 2, -3 and -5), indicating that the perturbations are temporally amplified. Consequently, types II and III solutions with $-5 \leq \alpha \leq 2$ are always unstable. Further, we note that $q \to -1$ as $R \to -\infty$ for type II solutions with $\alpha = 0$.

When $\alpha = 3$, the minimum decay rate (q) for a range of R is shown in Fig. 13. We note that the value of q for type I solutions is positive for $R_3^1 < R < \infty$, the least stable perturbations therefore decay with time and type I solutions (with $\alpha = 3$) are stable in this region. As opposed to type I solutions, the solutions of types II and III for $-\infty < R < R_3^2$ are unstable, since the perturbations are expected to grow in time as indicated by the negative value of q. Similarly, for type IV solutions, the value of q is negative for $R_3^1 < R < -0.796$ and hence type IV solutions are also unstable.

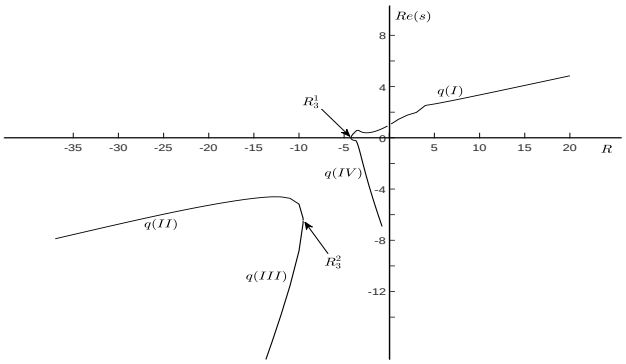

Figure 13: Real part (q) of the least stable eigenvalues for types I, II, III and IV solutions with $\alpha = 3$ under perturbations of general form.

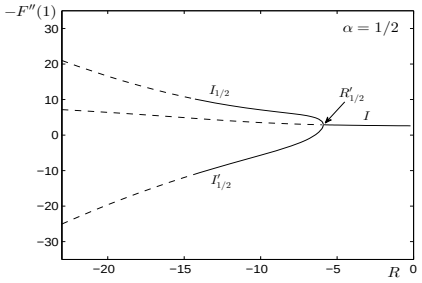

Figure 14: Values of $-F''(1)$ for the type I symmetric solutions, the asymmetric types $\mathrm{I}_{1/2}$ and $\mathrm{I}'_{1/2}$ solutions. The point marked $R'_{1/2}$ represents the pitch-fork bifurcation. The solid curves represent stable solutions, and the dashed curves represent unstable solutions.

Remark 3. *The vanishing of $q(I)$ suggests the existence of bifurcation. For example, in the case of $\alpha = 1/2$, the zero real eigenvalue at $R = R'_{1/2} = -5.905$ corresponds to a "pitch-fork" bifurcation. Two types of asymmetric steady solutions of (19) subject to (21) appear at $R'_{1/2}$ and form two branches of the "pitch-fork" bifurcation. We name the types of these solutions $I_{1/2}$ and $I'_{1/2}$*

(the mirror image of $I_{1/2}$ in the center line of the channel), and the results are shown in Fig. 14. The asymmetric solutions are characterized by a displacement of the stagnation point towards one of the walls. The axial velocity increases near this wall and decreases near the other one. This asymmetry effect increases with the decrease of cross-flow Reynolds number. When $R < -6.443$ there is a region close to one of the channel walls where the flow reverses. These asymmetric (types $I_{1/2}$ and $I'_{1/2}$) solutions are only stable for $-14.299 < R < R'_{1/2}$. Since we consider mainly the stability of the symmetric steady solutions, we will not expand this topic further here.

It is noted that we consider here not only perturbations of the similarity form (13), but also perturbations of the non-similarity (general) form. Although the linear stability (or instability) of the symmetric flows (with $-5 \leq \alpha \leq 3$) obtained here is the same as that under the perturbations of the similarity form shown in [1], the least stable eigenvalues or the most unstable eigenvalues are not all the same. For the case of $\alpha \neq 0$ and the case of $\alpha = 0$ and $R < 0$, the minimal real part of the eigenvalues (i.e., the minimum decay rate) of the perturbations for some flows is smaller than that of [1]; for the case of $\alpha = 0$ and $R > 0$, the maximal real part of the eigenvalues (i.e., the maximum growth rate) of the perturbations for some flows is larger than that of [1]. As a result, the least stable perturbations are expected to decay more slowly or grow faster. A few more examples are given below.

For type I solutions with $\alpha = -0.5$ and $-1 \leq R \leq -0.2$, the comparison of the least stable eigenvalues (i.e., the eigenvalues with the minimum decay rate) with those of [1] is shown in Table 4. In addition, the real parts of the streamwise velocity eigenfunction $\hat{u}(x, -0.00125)$ and the normal velocity eigenfunction $\hat{v}(x, 0)$ corresponding to the present results of the least stable eigenvalues (in Table 4) are illustrated in Fig. 15. The eigenvectors $\hat{\mathbf{v}}$ ($\hat{\mathbf{v}} = (\hat{u}_{\frac{3}{2},1}, \cdots, \hat{u}_{M-\frac{1}{2},N}, \hat{v}_{1,\frac{3}{2}}, \cdots, \hat{v}_{M,N-\frac{1}{2}})^T$) are normalised by using the corresponding 2-norm, so that the 2-norm of the eigenvectors is 1. It can be seen from Table 4 that the least stable eigenvalues for $R = -1$ and $R = -0.8$ are in

good agreement with those of [1]. For each case of $R = -1$ and $R = -0.8$, we note that the perturbation (corresponding to the least stable eigenvalue) is of the similarity form (13), and $\hat{u}(x, y)$ of streamwise velocity perturbation and $\hat{v}(x, y)$ of normal velocity perturbation are real functions. Therefore, $\hat{u}(x, -0.00125)$ plotted in Fig. 15(a) is proportional to x, and $\hat{v}(x, 0)$ plotted in Fig. 15(b) is independent of x. Nevertheless, in each case of $-0.6 \leq R \leq -0.2$, the minimum decay rate is smaller than that of [1] (see Table 4), implying that the corresponding least stable perturbation decays more slowly. Further, we note that the perturbation is not of the similarity form, since $Re(\hat{u}(x, -0.00125))$ plotted in Fig. 15(a) is not linear with respect to x, and $Re(\hat{v}(x, 0))$ plotted in Fig. 15(b) changes with x.

For type III solutions with $\alpha = 2$ and $-55 \leq R \leq -35$, Table 5 shows the comparison of the most unstable eigenvalues (i.e., the eigenvalues with the minimum decay rate) with those of [1]. In addition, the real parts of the streamwise velocity eigenfunction $\hat{u}(x, -0.00125)$ and the normal velocity eigenfunction $\hat{v}(x, 0)$ for the present results of the most unstable eigenvalues (in Table 5) are illustrated in Fig. 16. The eigenvectors $\hat{\mathbf{v}}$ are also normalized by using the corresponding 2-norm, and the 2-norm of the eigenvectors is 1. The most unstable eigenvalue for $R = -35$ is in good agreement with that of [1] (see Table 5). Moreover, the perturbation corresponding to this eigenvalue is of the similarity form. This is reflected in the results of the real parts of the eigenfunction components $\hat{u}(x, -0.00125)$ (plotted in Fig. 16(a)) and $\hat{v}(x, 0)$ (plotted in Fig. 16(b)) for $R = -35$. However, for each case of $-55 \leq R \leq -40$, the real part of the most unstable eigenvalue is smaller than that of [1] (see Table 5), indicating that the corresponding most unstable perturbation grows faster. Further, the perturbation is not of the similarity form as indicated by the results of the real parts of $\hat{u}(x, -0.00125)$ (plotted in Fig. 16(a)) and $\hat{v}(x, 0)$ (plotted in Fig. 16(b)) for $-55 \leq R \leq -40$.

Table 4: Comparison of the least stable eigenvalues for type I solutions with $\alpha = -0.5$ and various R ($-1 \leq R \leq -0.2$).

R	s of this paper	s of [1]
-1	8.54592635	8.54610042
-0.8	8.94762616	8.94779785
-0.6	9.10242071	9.35756576
-0.4	9.53456425	9.77561468
-0.2	$10.10359465 + 0.44475746i$	10.20215326

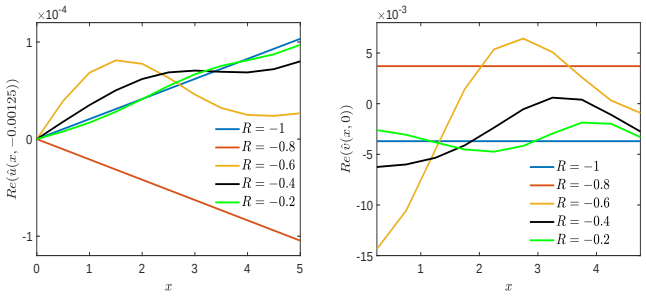

(a) (b)

Figure 15: Real part of components of the eigenfunction. (a) $\hat{u}(x, -0.00125)$ of streamwise velocity perturbation and (b) $\hat{v}(x, 0)$ of normal velocity perturbation. The results correspond to the least stable eigenvalues for type I solutions with $\alpha = -0.5$ and various Reynolds numbers R ($-1 \leq R \leq -0.2$) shown in Table 4.

Table 5: Comparison of the most unstable eigenvalues for type III solutions with $\alpha = 2$ and various R ($-55 \leq R \leq -35$).

R	s of this paper	s of [1]
-55	$-143.416051 + 75.392276i$	-141.404753
-50	$-128.696684 + 68.487956i$	-127.025993
-45	$-114.139808 + 61.875916i$	-113.025351
-40	$-99.705781 + 55.539635i$	-99.335182
-35	-85.871012	-85.871057

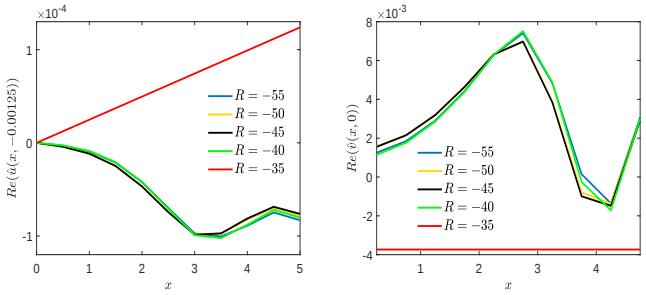

(a) (b)

Figure 16: Real part of components of the eigenfunction. (a) $\hat{u}(x, -0.00125)$ of streamwise velocity perturbation and (b) $\hat{v}(x, 0)$ of normal velocity perturbation. The results correspond to the most unstable eigenvalues for type III solutions with $\alpha = 2$ and various Reynolds numbers R ($-55 \leq R \leq -35$) shown in Table 5.

4. Non-linear analysis

The linear stability analysis is an approximate analysis but not necessarily always correct when long-time nonlinear dynamic systems are considered. As a validation of the linear stability results for the symmetric steady suction flow, we directly solve the original nonlinear time dependent problem (7), (8) subject to the boundary conditions (22)-(25). The initial condition is given as

$$\mathbf{v}(x, y, 0) = (xF_y + \varphi_1(x, y), -F + \varphi_2(x, y)), \tag{39}$$

where

$$(\varphi_1, \varphi_2) = (\varepsilon_1 sin(\xi_1 x + \eta_1 y + \theta_1), \varepsilon_2 sin(\xi_2 x + \eta_2 y + \theta_2)) \tag{40}$$

is a small initial perturbation for a given steady flow $(xF_y, -F)$. $(\varepsilon_1, \varepsilon_2)$ is the amplitude of the perturbation. (ξ_1, ξ_2) and (η_1, η_2) are the frequencies in x and y directions of the perturbation, respectively. We can choose different (θ_1, θ_2) for a sinusoidal or a cosine perturbation.

When $\alpha \neq 0$ and $R < 0$, a new variable $t^* = \frac{R}{2\alpha} ln(1 - \frac{2\alpha t}{R})$ is introduced so as to have a usual time interval $0 \leq t^* < \infty$. Substituting t^* into (7) and (8)

yields

$$\nabla \cdot \mathbf{v} = 0, \tag{41}$$

$$-\frac{\partial \mathbf{v}}{\partial t^*} - (\frac{\alpha}{R}x)\frac{\partial \mathbf{v}}{\partial x} - (\frac{\alpha}{R}y)\frac{\partial \mathbf{v}}{\partial y} - \frac{\alpha}{R}\mathbf{v} + \mathbf{v}\cdot\nabla\mathbf{v} = -\nabla p + \frac{1}{R}\triangle\mathbf{v}, \tag{42}$$

with the boundary conditions (22)-(25) and the initial condition (39).

We solve (41), (42) subject to (22)-(25) (where $x_r = 5$) and (39) by means of a finite difference method again. The spatial discretization makes use of the staggered mesh, and we consider a simple explicit discretization in time (see Appendix B). For the simplification of the presentation, the numerical results for a few selected α (i.e., $\alpha = -5$, $-1/2$, $1/2$ and 1) are provided. Other cases can all be calculated in the same way. Also for convenience, we only show the results for above problem with the initial perturbation $\varphi_1 = \varphi_2 = 0.0001sin(200x + 200y)$. We do test for various φ_1 and φ_2, and obtain the same stability results.

The time evolutions of the perturbed axial velocity ($u(4.5, y, t^*)/4.5$) of types I, II and III solutions (for some values of R and α) are displayed in Figs. 17, 18 and 19, respectively. The axial velocity profiles ($F'(y)$) of these steady flows are also shown (red solid lines). For type I solutions, the results are shown in Fig. 17. When $\alpha = -5$, for $R = -14.3$ (see Fig. 17(a)), we note that the curves do not change significantly with time, and can not be visually distinguished beyond $t^* = 10$, indicating that the steady flow of type I is stable at $R = -14.3$. Whereas for $R = -14.4$ (see Fig. 17(b)), the curves change into different forms over time, so the steady flow is unstable at $R = -14.4$. The other cases for $R > -14.3$ are also examined and the same results are obtained as that at $R = -14.3$. Thus, we can infer that there is a critical R between -14.4 and -14.3 for $\alpha = -5$. When $\alpha = -1/2$, for $R = -6.3$ (see Fig. 17(c)), the profiles beyond $t^* = 10$ become indiscernible, signifying the steady flow is stable at this R. Whereas for $R = -6.4$ (see Fig. 17(d)), with the time evolution, the axial velocity increases near the lower wall and decreases near the upper wall. When the time exceeds $t^* = 1200$, the axial velocity does not change. That is, the flow evolves into a new asymmetric steady state. Therefore, the symmetric flow of type I at $R = -6.4$ is unstable. The flows for $R > -6.3$ are also examined and

appear to be stable. Thus, we can obtain that a critical R exists between -6.4 and -6.3 for $\alpha = -1/2$. Similarly, when $\alpha = 1/2$, it can be seen from Fig. 17(e) that the axial velocity at $R = -5.9$ does not change significantly with time. While the axial velocity at $R = -6$ shown in Fig. 17(f) increases near the lower wall and decreases near the upper wall with time, and the flow finally turns into an asymmetric steady flow (i.e., the flow of type $\mathrm{I}'_{1/2}$). This indicates that the stability changes between $R = -6$ and $R = -5.9$. When $\alpha = 1$, the results for $R = -10$ and -50 are shown in Figs. 17(g) and 17(h), respectively. As time goes on, the curves of each solution become indistinguishable, indicating that the two steady solutions of type I are stable.

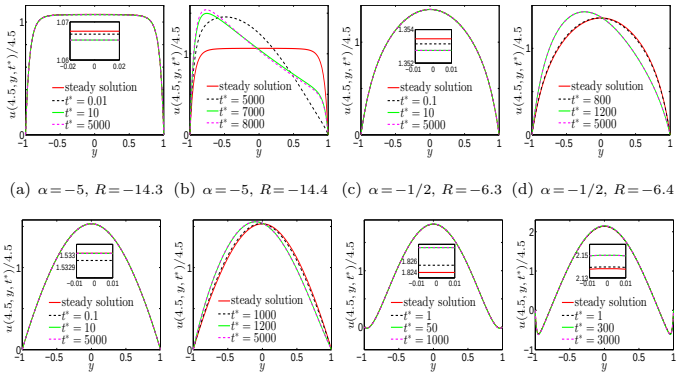

(a) $\alpha = -5$, $R = -14.3$ (b) $\alpha = -5$, $R = -14.4$ (c) $\alpha = -1/2$, $R = -6.3$ (d) $\alpha = -1/2$, $R = -6.4$

(e) $\alpha = 1/2$, $R = -5.9$ (f) $\alpha = 1/2$, $R = -6$ (g) $\alpha = 1$, $R = -10$ (h) $\alpha = 1$, $R = -50$

Figure 17: Spatial variations of the perturbed axial velocity $u(4.5, y, t^*)/4.5$ for some values of t^*, and the corresponding axial velocity profiles $F'(y)$ of the steady solutions of type I for some values of α and R: (a) $\alpha = -5$, $R = -14.3$, (b) $\alpha = -5$, $R = -14.4$, (c) $\alpha = -1/2$, $R = -6.3$, (d) $\alpha = -1/2$, $R = -6.4$, (e) $\alpha = 1/2$, $R = -5.9$, (f) $\alpha = 1/2$, $R = -6$, (g) $\alpha = 1$, $R = -10$, and (h) $\alpha = 1$, $R = -50$.

For types II and III solutions of each case of $-5 \le \alpha \le 1$ (i.e., $\alpha = -5$, $-1/2$, $1/2$ and 1), the numerical simulations are performed for a certain R near which the solutions appear, and the results are shown in Figs. 18 and 19. For $\alpha = -5$

and $R = -14.5$ (in Figs. 18(a) and 19(a)), we note that with the time evolution, the profiles change constantly and tend to the profile of type I solution that we have discussed before. For $\alpha = -1/2$ and $R = -12.6$, as illustrated in Figs. 18(b) and 19(b), as time goes, flow reversals gradually transfer from the center of the channel to the lower and upper walls, respectively. The flows ultimately turn into two different asymmetric steady states (which are mirror images of each other in the center line of the channel). For $\alpha = 1/2$ and $R = -11.8$ (in Figs. 18(c) and 19(c)), as time goes, the flow reversals first transfer from the center of the channel to the upper and lower walls, and then gradually disappear from the upper wall of the channel. The flows of types II and III eventually become the same asymmetric steady flow (i.e., the flow of type $\mathrm{I}_{1/2}$) with flow reversal being only near the lower wall. For $\alpha = 1$ and $R = -11.3$ (in Figs. 18(d) and 19(d)), it can be seen that after a period of time, the flows of types II and III turn into the symmetric steady flow of type I.

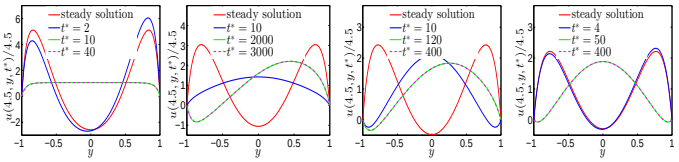

(a) $\alpha = -5$, $R = -14.5$ (b) $\alpha = -1/2$, $R = -12.6$ (c) $\alpha = 1/2$, $R = -11.8$ (d) $\alpha = 1$, $R = -11.3$

Figure 18: Spatial variations of the perturbed axial velocity $u(4.5, y, t^*)/4.5$ for some values of t^*, and the corresponding axial velocity profiles $F'(y)$ of the steady solutions of type II for some values of α and R: (a) $\alpha = -5$, $R = -14.5$, (b) $\alpha = -1/2$, $R = -12.6$, (c) $\alpha = 1/2$, $R = -11.8$, and (d) $\alpha = 1$, $R = -11.3$.

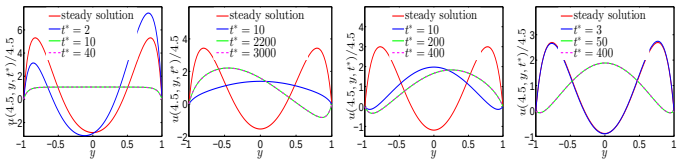

(a) $\alpha=-5$, $R=-14.5$ (b) $\alpha=-1/2$, $R=-12.6$ (c) $\alpha=1/2$, $R=-11.8$ (d) $\alpha=1$, $R=-11.3$

Figure 19: Spatial variations of the perturbed axial velocity $u(4.5, y, t^*)/4.5$ for some values of t^*, and the corresponding axial velocity profiles $F'(y)$ of the steady solutions of type III for some values of α and R: (a) $\alpha = -5$, $R = -14.5$, (b) $\alpha = -1/2$, $R = -12.6$, (c) $\alpha = 1/2$, $R = -11.8$, and (d) $\alpha = 1$, $R = -11.3$.

5. Conclusion

In this numerical study, the multiple symmetric similarity solutions of a flow problem occurring in a uniformly porous channel with expanding (or contracting) walls are considered in a range of the wall expansion ratios α, say, $[-5, 3]$. We examine the linear temporal stability of these solutions under perturbations of general form (including similarity and non-similarity forms). Through a finite difference method on a staggered grid we solve two-dimensional eigenvalue problems associated with the linear stability analysis and the stability of these solutions is then obtained. That is, type I solutions in each case of $-5 \le \alpha \le 1/2$ are only stable for a range of R (cross-flow Reynolds number), and type I solutions with $1 \le \alpha \le 3$ are stable for all R where they exist. Further, it is found that for $\alpha < 0$ (in the case of wall contraction), the stable region of R increases as the contraction ratio ($|\alpha|$) increases; for $0 < \alpha \le 1$ (in the case of wall expansion), the stable region increases as the expansion ratio (α) increases. So the expansion ratio α has a great influence on the stability of the flows of type I, and it seems that the presence of an inflection point of axial velocity (or the flow acceleration changes from decrease to increase) near the wall may stabilize the flow. In addition, other types of flows whose axial velocity profiles have an inflection point near the center of the channel are always unstable, suggesting

that these flows may transition to turbulence prior to physically attaining these shapes. In other words, these flows may not be physically observable.

Although the stability (or instability) of these steady flows obtained here under perturbations of general form is the same as that under the perturbations of the similarity form shown in [1], the minimum decay rate or maximum growth rate of the perturbations are not all the same. For the case of $\alpha \neq 0$ and the case of $\alpha = 0$ and $R < 0$, the minimal real part of the eigenvalues (i.e., the minimum decay rate) of the perturbations for some flows is smaller than that of [1]; for the case of $\alpha = 0$ and $R > 0$, the maximal real part of the eigenvalues (i.e., the maximum growth rate) of the perturbations for some flows is larger than that of [1]. As a result, the least stable perturbations are expected to decay more slowly or grow faster.

On the other hand, non-linear analysis has been carried out by directly solving the original nonlinear time dependent problem with an initial perturbation of general form. It is found that the stability results agree well with those obtained from the linear stability analysis.

Acknowledgements

This work is partially supported by the National Natural Science Foundation of China (Nos. 11771040, 12001035 and 11861131004) and the Fundamental Research Funds for the Central Universities (No. 06500073). Z. G. acknowledges support from the NSAF grant in National Natural Science Foundation of China with grant No. U1930402.

APPENDIX A: Discretization of eigenvalue problem

Discretization of the eigenvalue problem (37) (for $\alpha > 0$) associated with (38) is based on a finite difference method with the staggered grid (Fig. 20)

[27]. The finite difference scheme is as following:

$$\begin{cases}
-(\frac{\hat{u}_{i+\frac{3}{2},j}-2\hat{u}_{i+\frac{1}{2},j}+\hat{u}_{i-\frac{1}{2},j}}{h^2}+\frac{\hat{u}_{i+\frac{1}{2},j+1}-2\hat{u}_{i+\frac{1}{2},j}+\hat{u}_{i+\frac{1}{2},j-1}}{k^2}) \\
-(\alpha x_{i+\frac{1}{2}})(\frac{\hat{u}_{i+\frac{3}{2},j}-\hat{u}_{i-\frac{1}{2},j}}{2h})-(\alpha y_j)(\frac{\hat{u}_{i+\frac{1}{2},j+1}-\hat{u}_{i+\frac{1}{2},j-1}}{2k})-\alpha\hat{u}_{i+\frac{1}{2},j} \\
+R(F'_j\hat{u}_{i+\frac{1}{2},j}+x_{i+\frac{1}{2}}F''_j\hat{v}_{i+\frac{1}{2},j})+R(x_{i+\frac{1}{2}}F'_j(\frac{\hat{u}_{i+\frac{3}{2},j}-\hat{u}_{i-\frac{1}{2},j}}{2h})-F_j(\frac{\hat{u}_{i+\frac{1}{2},j+1}-\hat{u}_{i+\frac{1}{2},j-1}}{2k})) \\
+R(\frac{\hat{p}_{i+1,j}-\hat{p}_{i,j}}{h}) \\
=2\alpha s\hat{u}_{i+\frac{1}{2},j}, \qquad i=1,\cdots,M-1, \quad j=1,\cdots,N \\
-(\frac{\hat{v}_{i+1,j+\frac{1}{2}}-2\hat{v}_{i,j+\frac{1}{2}}+\hat{v}_{i-1,j+\frac{1}{2}}}{h^2}+\frac{\hat{v}_{i,j+\frac{3}{2}}-2\hat{v}_{i,j+\frac{1}{2}}+\hat{v}_{i,j-\frac{1}{2}}}{k^2}) \\
-(\alpha x_i)(\frac{\hat{v}_{i+1,j+\frac{1}{2}}-\hat{v}_{i-1,j+\frac{1}{2}}}{2h})-(\alpha y_{j+\frac{1}{2}})(\frac{\hat{v}_{i,j+\frac{3}{2}}-\hat{v}_{i,j-\frac{1}{2}}}{2k})-\alpha\hat{v}_{i,j+\frac{1}{2}} \\
+R(-F'_{j+\frac{1}{2}}\hat{v}_{i,j+\frac{1}{2}})+R(x_iF'_{j+\frac{1}{2}}(\frac{\hat{v}_{i+1,j+\frac{1}{2}}-\hat{v}_{i-1,j+\frac{1}{2}}}{2h})-F_{j+\frac{1}{2}}(\frac{\hat{v}_{i,j+\frac{3}{2}}-\hat{v}_{i,j-\frac{1}{2}}}{2k})) \\
+R(\frac{\hat{p}_{i,j+1}-\hat{p}_{i,j}}{k}) \\
=2\alpha s\hat{v}_{i,j+\frac{1}{2}}, \qquad i=1,\cdots,M, \quad j=1,\cdots,N-1 \\
\frac{\hat{u}_{i+\frac{1}{2},j}-\hat{u}_{i-\frac{1}{2},j}}{h}+\frac{\hat{v}_{i,j+\frac{1}{2}}-\hat{v}_{i,j-\frac{1}{2}}}{k}=0, \qquad i=1,\cdots,M, \quad j=1,\cdots,N
\end{cases} \tag{A1}$$

$$\begin{cases}
\frac{\hat{u}_{i+\frac{1}{2},N+1}+\hat{u}_{i+\frac{1}{2},N}}{2}=0, \quad \hat{v}_{i,N+\frac{1}{2}}=0, \quad i=1,\cdots,M \\
\frac{\hat{u}_{i+\frac{1}{2},1}+\hat{u}_{i+\frac{1}{2},0}}{2}=0, \quad \hat{v}_{i,\frac{1}{2}}=0, \quad i=1,\cdots,M \\
\hat{u}_{\frac{1}{2},j}=0, \qquad \frac{\hat{v}_{1,j+\frac{1}{2}}-\hat{v}_{0,j+\frac{1}{2}}}{h}=0, \quad j=1,\cdots,N \\
\hat{u}_{M+\frac{1}{2},j}-x_r\frac{\hat{u}_{M+\frac{1}{2},j}-\hat{u}_{M-\frac{1}{2},j}}{h}=0, \qquad \frac{\hat{v}_{M+1,j+\frac{1}{2}}-\hat{v}_{M,j+\frac{1}{2}}}{h}=0, \quad j=1,\cdots,N
\end{cases} \tag{A2}$$

where $\hat{v}_{i+\frac{1}{2},j}=\frac{1}{4}(\hat{v}_{i,j+\frac{1}{2}}+\hat{v}_{i+1,j+\frac{1}{2}}+\hat{v}_{i,j-\frac{1}{2}}+\hat{v}_{i+1,j-\frac{1}{2}})$, h and k are grid sizes. The set of grid points in the xy plane is given by $(x_i,y_j)=((i-\frac{1}{2})h,-1+(j-\frac{1}{2})k)$, where i, j are integers. $\hat{u}_{i+\frac{1}{2},j}$, $\hat{v}_{i,j+\frac{1}{2}}$ and $\hat{p}_{i,j}$ are the approximations of $\hat{u}(ih,-1+(j-\frac{1}{2})k)$, $\hat{v}((i-\frac{1}{2})h,-1+jk)$ and $\hat{p}((i-\frac{1}{2})h,-1+(j-\frac{1}{2})k)$.

To fix an arbitrary constant associated with the solution of the pressure, without losing generality, we let $\hat{p}_{1,1}=0$ and ignore the first discretized conti-

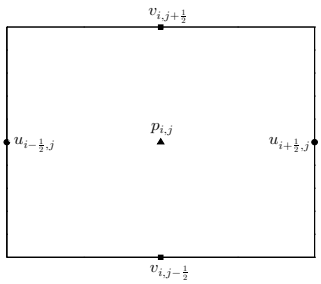

Figure 20: The staggered grid.

nuity equation with $i = 1$ and $j = 1$. Then we can write the eigenvalue problem into the matrix vector form:

$$A\hat{\mathbf{v}} + B\hat{\mathbf{p}} = s\hat{\mathbf{v}}, \tag{A3}$$

$$W\hat{\mathbf{v}} = 0, \tag{A4}$$

where $\hat{\mathbf{v}} = (\hat{u}_{\frac{3}{2},1}, \cdots, \hat{u}_{M-\frac{1}{2},N}, \hat{v}_{1,\frac{3}{2}}, \cdots, \hat{v}_{M,N-\frac{1}{2}})^T$, $\hat{\mathbf{p}} = (\hat{p}_{2,1}, \cdots, \hat{p}_{M,N})^T$, A is an $n\times n$ matrix, B is an $n\times m$ matrix of rank m and W an $m\times n$ matrix of rank m. Here, $n = (M-1)\times N + M\times(N-1)$ and $m = M\times N-1$. Following the approach in [28, 29], do QR decomposition of W^T: $W^T = QR = [Q_1, Q_2]R = Q_1R_1$, where Q is $n \times n$ orthogonal, Q_1 is $n \times m$, Q_2 is $n \times (n - m)$, R is $n \times m$ and R_1 (which is composed of the first m rows of R) is $m \times m$ nonsingular and upper triangular. Eliminating $\hat{\mathbf{p}}$ using $W\hat{\mathbf{v}} = 0$, we thus essentially obtain the eigenvalue problem $Q_2^T(A - B(Q_1^TB)^{-1}Q_1^TA)Q_2\mathbf{z} = s\mathbf{z}$, where $\mathbf{z} = Q_2^T\hat{\mathbf{v}}$.

Therefore, the original eigenvalue problem has precisely $n - m$ eigenvalues, which can be obtained by solving the eigenvalues of the matrix $Q_2^T(A - B(Q_1^TB)^{-1}Q_1^TA)Q_2$.

APPENDIX B: Discretization of original nonlinear time dependent problem

The approximation of (41) and (42) is

$$
\begin{cases}
-(\frac{u^{n+1}_{i+\frac{1}{2},j}-u^{n}_{i+\frac{1}{2},j}}{\tau})-\frac{\alpha}{R}(x_{i+\frac{1}{2}})(\frac{u^{n+1}_{i+\frac{3}{2},j}-u^{n+1}_{i-\frac{1}{2},j}}{2h}) \\
-\frac{\alpha}{R}(y_j)(\frac{u^{n+1}_{i+\frac{1}{2},j+1}-u^{n+1}_{i+\frac{1}{2},j-1}}{2k})-\frac{\alpha}{R}u^{n+1}_{i+\frac{1}{2},j}+u^{n}_{i+\frac{1}{2},j}(\frac{u^{n}_{i+\frac{3}{2},j}-u^{n}_{i-\frac{1}{2},j}}{2h}) \\
+v^{n}_{i+\frac{1}{2},j}(\frac{u^{n}_{i+\frac{1}{2},j+1}-u^{n}_{i+\frac{1}{2},j-1}}{2k})+(\frac{p^{n+1}_{i+1,j}-p^{n+1}_{i,j}}{h}) \\
-\frac{1}{R}(\frac{u^{n+1}_{i+\frac{3}{2},j}-2u^{n+1}_{i+\frac{1}{2},j}+u^{n+1}_{i-\frac{1}{2},j}}{h^2}+\frac{u^{n+1}_{i+\frac{1}{2},j+1}-2u^{n+1}_{i+\frac{1}{2},j}+u^{n+1}_{i+\frac{1}{2},j-1}}{k^2})=0, \\
i=1,\cdots,M-1, \quad j=1,\cdots,N \\
-(\frac{v^{n+1}_{i,j+\frac{1}{2}}-v^{n}_{i,j+\frac{1}{2}}}{\tau})-\frac{\alpha}{R}(x_i)(\frac{v^{n+1}_{i+1,j+\frac{1}{2}}-v^{n+1}_{i-1,j+\frac{1}{2}}}{2h}) \\
-\frac{\alpha}{R}(y_{j+\frac{1}{2}})(\frac{v^{n+1}_{i,j+\frac{3}{2}}-v^{n+1}_{i,j-\frac{1}{2}}}{2k})-\frac{\alpha}{R}v^{n+1}_{i,j+\frac{1}{2}}+u^{n}_{i,j+\frac{1}{2}}(\frac{v^{n}_{i+1,j+\frac{1}{2}}-v^{n}_{i-1,j+\frac{1}{2}}}{2h}) \\
+v^{n}_{i,j+\frac{1}{2}}(\frac{v^{n}_{i,j+\frac{3}{2}}-v^{n}_{i,j-\frac{1}{2}}}{2k})+(\frac{p^{n+1}_{i,j+1}-p^{n+1}_{i,j}}{k}) \\
-\frac{1}{R}(\frac{v^{n+1}_{i+1,j+\frac{1}{2}}-2v^{n+1}_{i,j+\frac{1}{2}}+v^{n+1}_{i-1,j+\frac{1}{2}}}{h^2}+\frac{v^{n+1}_{i,j+\frac{3}{2}}-2v^{n+1}_{i,j+\frac{1}{2}}+v^{n+1}_{i,j-\frac{1}{2}}}{k^2})=0, \\
i=1,\cdots,M, \quad j=1,\cdots,N-1 \\
\frac{u^{n+1}_{i+\frac{1}{2},j}-u^{n+1}_{i-\frac{1}{2},j}}{h}+\frac{v^{n+1}_{i,j+\frac{1}{2}}-v^{n+1}_{i,j-\frac{1}{2}}}{k}=0, \qquad i=1,\cdots,M, \quad j=1,\cdots,N
\end{cases}
$$

where $v^{n}_{i+\frac{1}{2},j}=\frac{1}{4}(v^{n}_{i,j+\frac{1}{2}}+v^{n}_{i+1,j+\frac{1}{2}}+v^{n}_{i,j-\frac{1}{2}}+v^{n}_{i+1,j-\frac{1}{2}})$, $u^{n}_{i,j+\frac{1}{2}}=\frac{1}{4}(u^{n}_{i-\frac{1}{2},j}+u^{n}_{i+\frac{1}{2},j}+u^{n}_{i-\frac{1}{2},j+1}+u^{n}_{i+\frac{1}{2},j+1})$. The boundary conditions (22)-(25) (where $x_r=5$)

are interpreted as

$$\begin{cases} \dfrac{u^{n+1}_{i+\frac{1}{2},N+1}+u^{n+1}_{i+\frac{1}{2},N}}{2}=0, \quad v^{n+1}_{i,N+\frac{1}{2}}=-1, & i=1,\cdots,M \\ \dfrac{u^{n+1}_{i+\frac{1}{2},1}+u^{n+1}_{i+\frac{1}{2},0}}{2}=0, \quad v^{n+1}_{i,\frac{1}{2}}=1, & i=1,\cdots,M \\ u^{n+1}_{\frac{1}{2},j}=0, \quad \dfrac{v^{n+1}_{1,j+\frac{1}{2}}-v^{n+1}_{0,j+\frac{1}{2}}}{h}=0, & j=1,\cdots,N \\ u^{n+1}_{M+\frac{1}{2},j}-5\dfrac{u^{n+1}_{M+\frac{1}{2},j}-u^{n+1}_{M-\frac{1}{2},j}}{h}=0, & j=1,\cdots,N \\ \dfrac{v^{n+1}_{M+1,j+\frac{1}{2}}-v^{n+1}_{M,j+\frac{1}{2}}}{h}=0, & j=1,\cdots,N \end{cases}$$

and the initial condition (39) is interpreted as

$$\begin{cases} u^0_{i+\frac{1}{2},j}=x_{i+\frac{1}{2}}F'_j+(\varphi_1)_{i+\frac{1}{2},j}, \quad i=1,\cdots,M-1, \quad j=1,\cdots,N \\ v^0_{i,j+\frac{1}{2}}=-F_{j+\frac{1}{2}}+(\varphi_2)_{i,j+\frac{1}{2}}, \qquad i=1,\cdots,M, \quad j=1,\cdots,N-1 \end{cases}$$

where h and k are the dimensions of the grids, and τ is the time increment. $u^{n+1}_{i+\frac{1}{2},j}$, $v^{n+1}_{i,j+\frac{1}{2}}$ and $p^{n+1}_{i,j}$ are the approximations of $u(ih,-1+(j-\frac{1}{2})k)$, $v((i-\frac{1}{2})h,-1+jk)$ and $p((i-\frac{1}{2})h,-1+(j-\frac{1}{2})k)$ at the time $t^*=(n+1)\tau$, where $n=0,1,2,\cdots$. We impose $p^{n+1}_{1,1}=0$ as before to fix the arbitrary constant associated with the pressure solution. In the meantime, the discretized continuity equations for $i=1$, $j=1$ are ignored. Then the unknown values at time $n+1$ are uniquely determined and can be solved step by step.

Data availability

The data that support the findings of this study are available from the corresponding author upon reasonable request.

References

[1] Y. Sun, P. Lin, L. Li, Temporal stability analysis for multiple similarity solutions of viscous incompressible flows in porous channels with moving walls, Applied Mathematical Modelling 77 (2020) 738 – 755.

[2] E. C. Dauenhauer, J. Majdalani, Exact self-similarity solution of the navier-stokes equations for a porous channel with orthogonally moving walls, Physics of Fluids 15 (6) (2003) 1485–1495. doi:10.1063/1.1567719.

[3] C. Zhou, J. Majdalani, Improved mean-flow solution for slab rocket motors with regressing walls, Journal of Propulsion and Power 18 (3) (2002) 703–711. doi:10.2514/2.5987.

[4] J. Majdalani, C. Zhou, C. A. Dawson, Two-dimensional viscous flow between slowly expanding or contracting walls with weak permeability, Journal of Biomechanics 35 (10) (2002) 1399–1403. doi:10.1016/S0021-9290(02)00186-0.

[5] A. S. Berman, Laminar flow in channels with porous walls, Journal of Applied Physics 24 (9) (1953) 1232–1235. doi:10.1063/1.1721476.

[6] R. M. Terrill, Laminar flow in a uniformly porous channel, Aeronautical Quarterly 15 (1964) 299–310.

[7] I. Proudman, An example of steady laminar flow at large Reynolds number, Journal of Fluid Mechanics 9 (4) (1960) 593–602.

[8] M. Morduchow, On laminar flow through a channel or tube with injection: Application of method of averages, Quarterly of Applied Mathematics 14 (4) (1957) 361–368.

[9] S. W. Yuan, Further investigation of laminar flow in channels with porous walls, Journal of Applied Physics 27 (3) (1956) 267–269.

[10] R. M. Terrill, Laminar flow in a uniformly porous channel with large injection, Aeronautical Quarterly 16 (4) (1965) 323–332. doi:10.1017/S0001925900003565.

[11] J. F. Brady, A. Acrivos, Steady flow in a channel or tube with an accelerating surface velocity. An exact solution to the Navier-Stokes equations with reverse flow, Journal of Fluid Mechanics 112 (1981) 127–150. doi:10.1017/S0022112081000323.

[12] J. Majdalani, C. Zhou, Moderate-to-large injection and suction driven channel flows with expanding or contracting walls, ZAMM - Journal of Applied Mathematics and Mechanics / Zeitschrift für Angewandte Mathematik und Mechanik 83 (3) (2003) 181–196. doi:10.1002/zamm.200310018.

[13] H. Xu, Z.-L. Lin, S.-J. Liao, J.-Z. Wu, J. Majdalani, Homotopy based solutions of the navier-stokes equations for a porous channel with orthogonally moving walls, Physics of Fluids 22 (5) (2010) 053601. doi:10.1063/1.3392770.

[14] J. Majdalani, L.-J. Xuan, On the viscous core boundary layer of the injection and suction driven channel flows with expanding or contracting walls, ZAMM - Journal of Applied Mathematics and Mechanics / Zeitschrift für Angewandte Mathematik und Mechanik 98 (6) (2018) 969–980.

[15] Q.-B. Chen, H. Xu, Coiflet wavelet-homotopy solution of channel flow due to orthogonally moving porous walls governed by the Navier-Stokes equations, Journal of Mathematics 2020.

[16] T. Saad, J. Majdalani, Viscous mean flow approximations for porous tubes with radially regressing walls, AIAA Journal 55 (11) (2017) 3868–3880.

[17] L. Durlofsky, J. F. Brady, The spatial stability of a class of similarity solutions, Physics of Fluids 27 (5) (1984) 1068–1076. doi:10.1063/1.864736.

[18] S. Ferro, G. Gnavi, Spatial stability of similarity solutions for viscous flows in channels with porous walls, Physics of Fluids 12 (4) (2000) 797–802. doi:10.1063/1.870336.

[19] M. B. Zaturska, P. G. Drazin, W. H. H. Banks, On the flow of a viscous fluid driven along a channel by suction at porous walls, Fluid Dynamics Research 4 (3) (1988) 151–178.

[20] C. L. Taylor, W. H. H. Banks, M. B. Zaturska, P. G. Drazin, Three-dimensional flow in a porous channel, The Quarterly Journal of Mechanics and Applied Mathematics 44 (1) (1991) 105–133.

[21] E. B. B. Watson, W. H. H. Banks, M. B. Zaturska, P. G. Drazin, On transition to chaos in two-dimensional channel flow symmetrically driven by accelerating walls, Journal of Fluid Mechanics 212 (1990) 451–485.

[22] F. Chedevergne, G. Casalis, J. Majdalani, Direct numerical simulation and biglobal stability investigations of the gaseous motion in solid rocket motors, Journal of Fluid Mechanics 706 (2012) 190–218.

[23] G. Boyer, G. Casalis, J.-L. Estivalèzes, Stability analysis and numerical simulation of simplified solid rocket motors, Physics of Fluids 25 (8) (2013) 084109.

[24] Y. Li, Z. Wang, P. Liu, On the grid dependence of hydrodynamic stability analysis in solid rocket motors, Physics of Fluids 32 (3) (2020) 034103.

[25] K. H. Yu, C. J. Teo, B. C. Khoo, Linear stability of pressure-driven flow over longitudinal superhydrophobic grooves, Physics of Fluids 28 (2) (2016) 022001.

[26] T.-Y. Qi, C. Liu, M.-J. Ni, J.-C. Yang, The linear stability of hunt-rayleigh-bénard flow, Physics of Fluids 29 (6) (2017) 064103.

[27] F. H. Harlow, J. E. Welch, Numerical calculation of time-dependent viscous incompressible flow of fluid with free surface, The Physics of Fluids 8 (12) (1965) 2182–2189.

[28] K. A. Cliffe, T. J. Garratt, A. Spence, Eigenvalues of block matrices arising from problems in fluid mechanics, SIAM Journal on Matrix Analysis and Applications 15 (4) (1994) 1310–1318. doi:10.1137/S0895479892233230.

[29] K. A. Cliffe, T. J. Garratt, A. Spence, Eigenvalues of the discretized Navier-Stokes equation with application to the detection of Hopf bifurcations, Advances in Computational Mathematics 1 (1993) 337–356.

PLEASE CITE THIS ARTICLE AS DOI: 10.1063/5.0051846

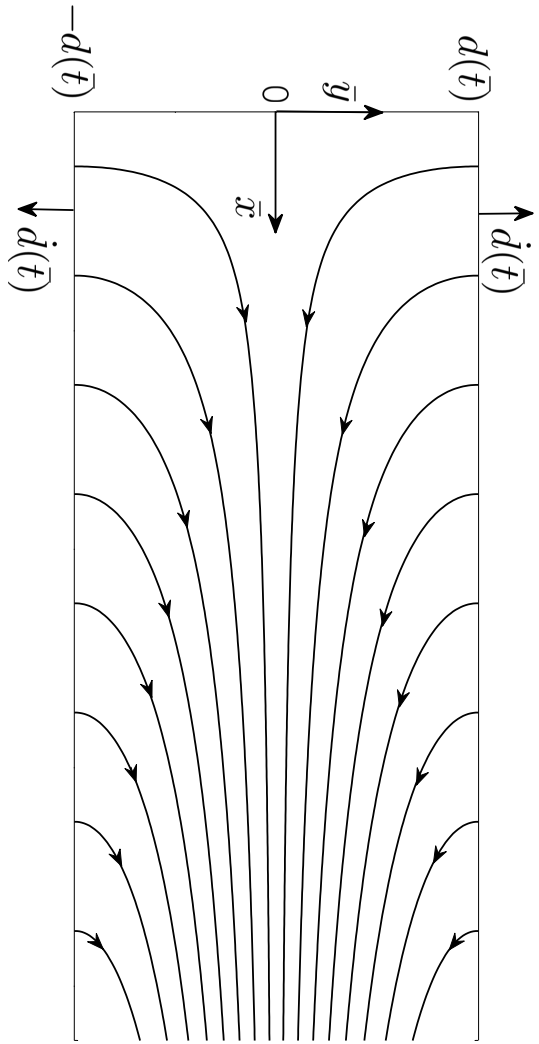

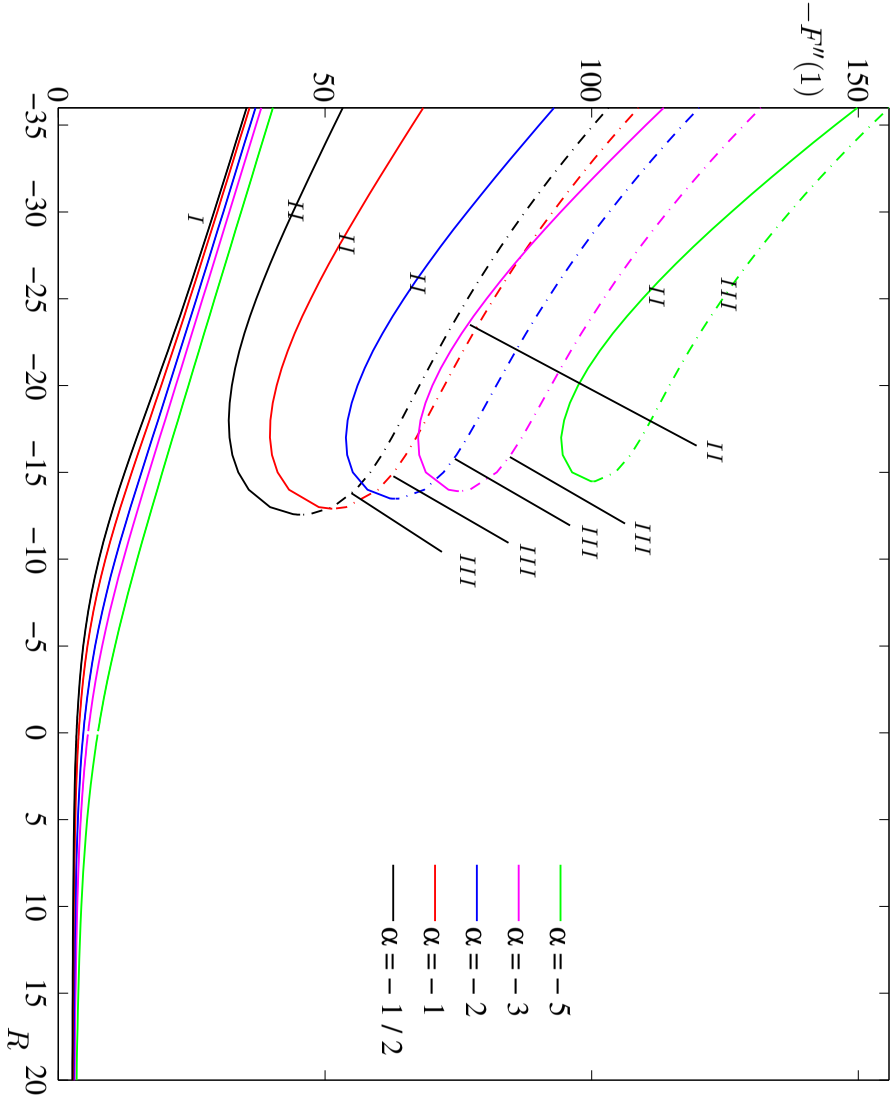

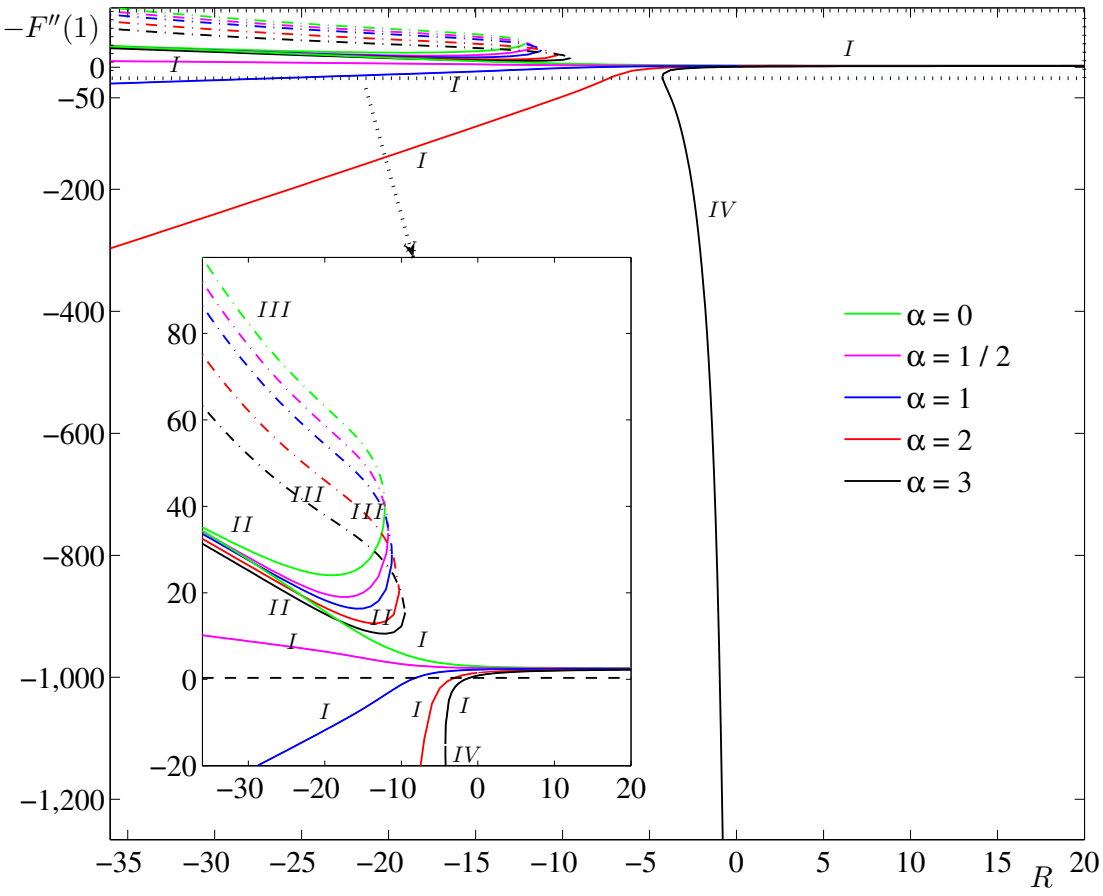

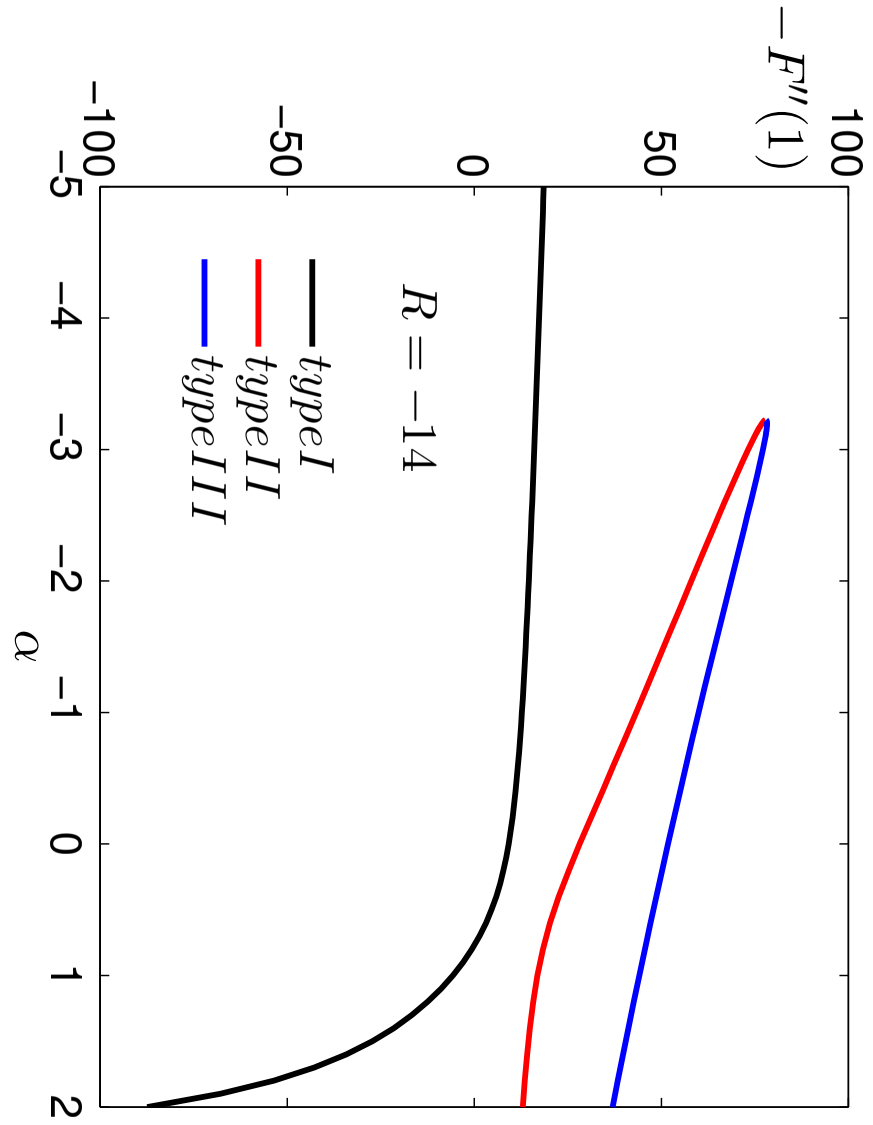

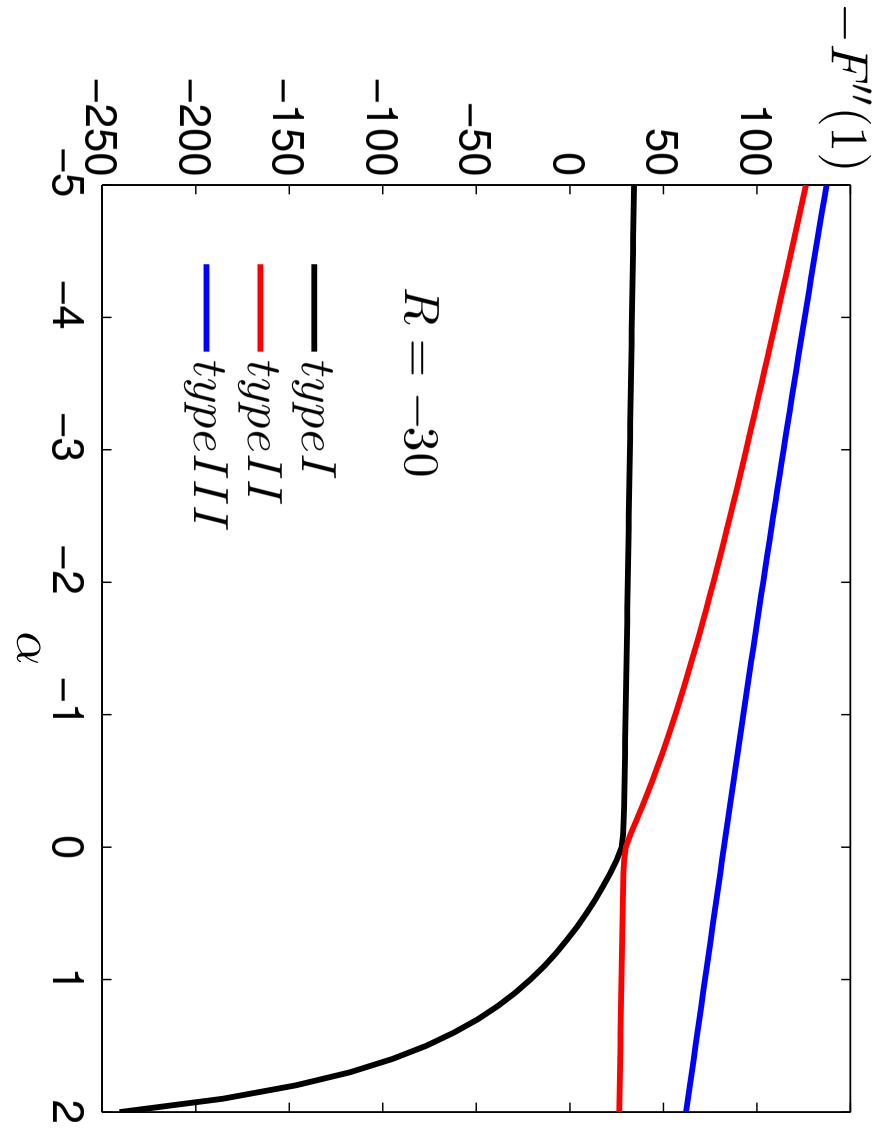

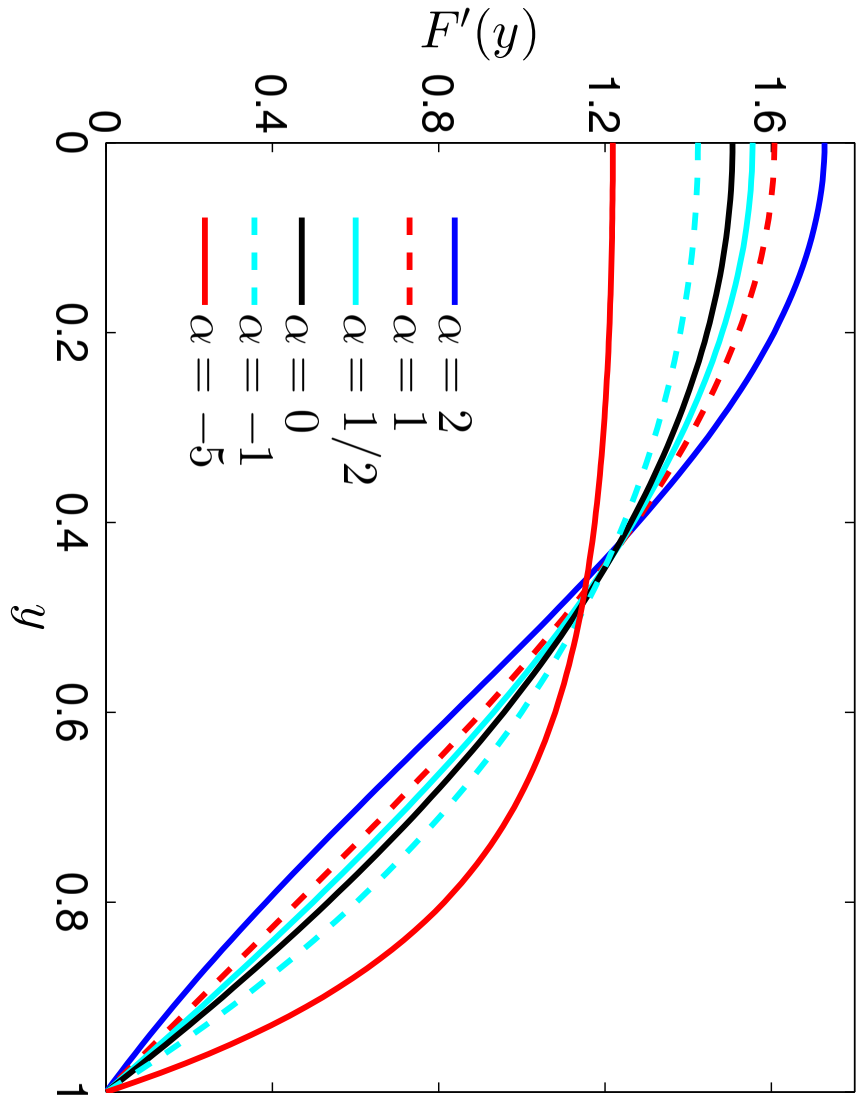

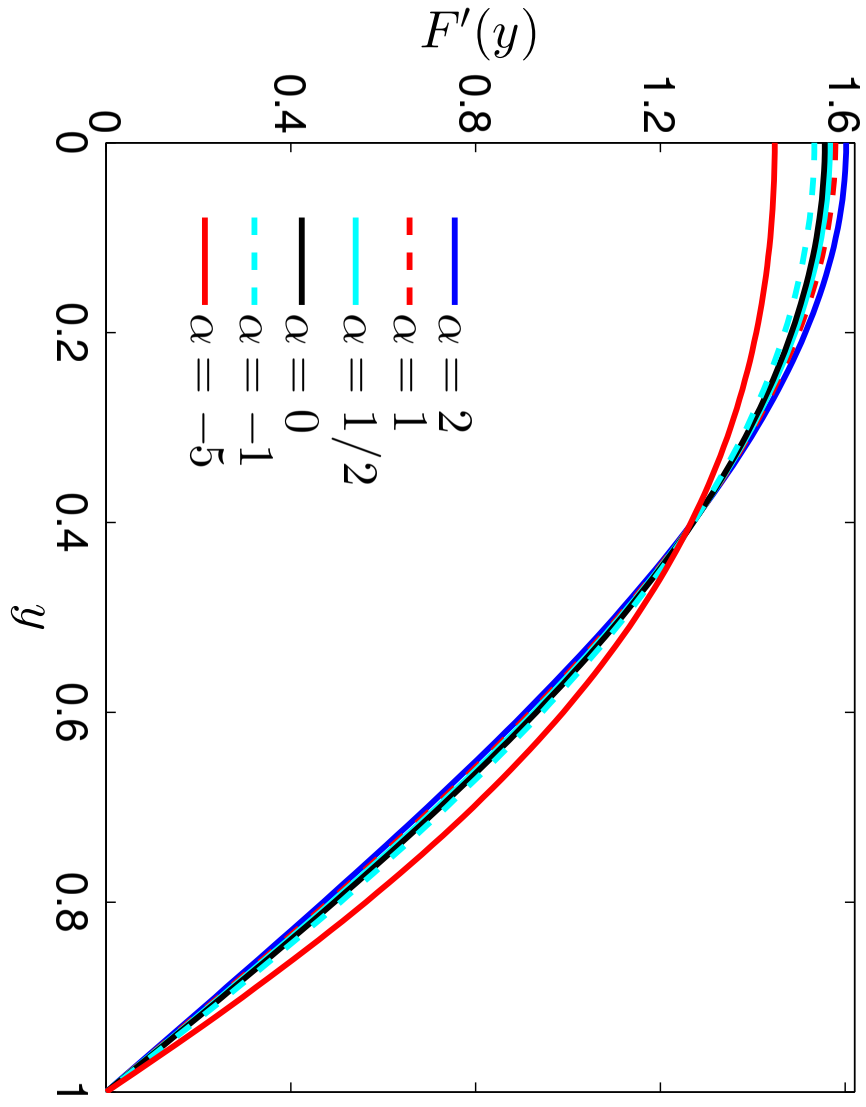

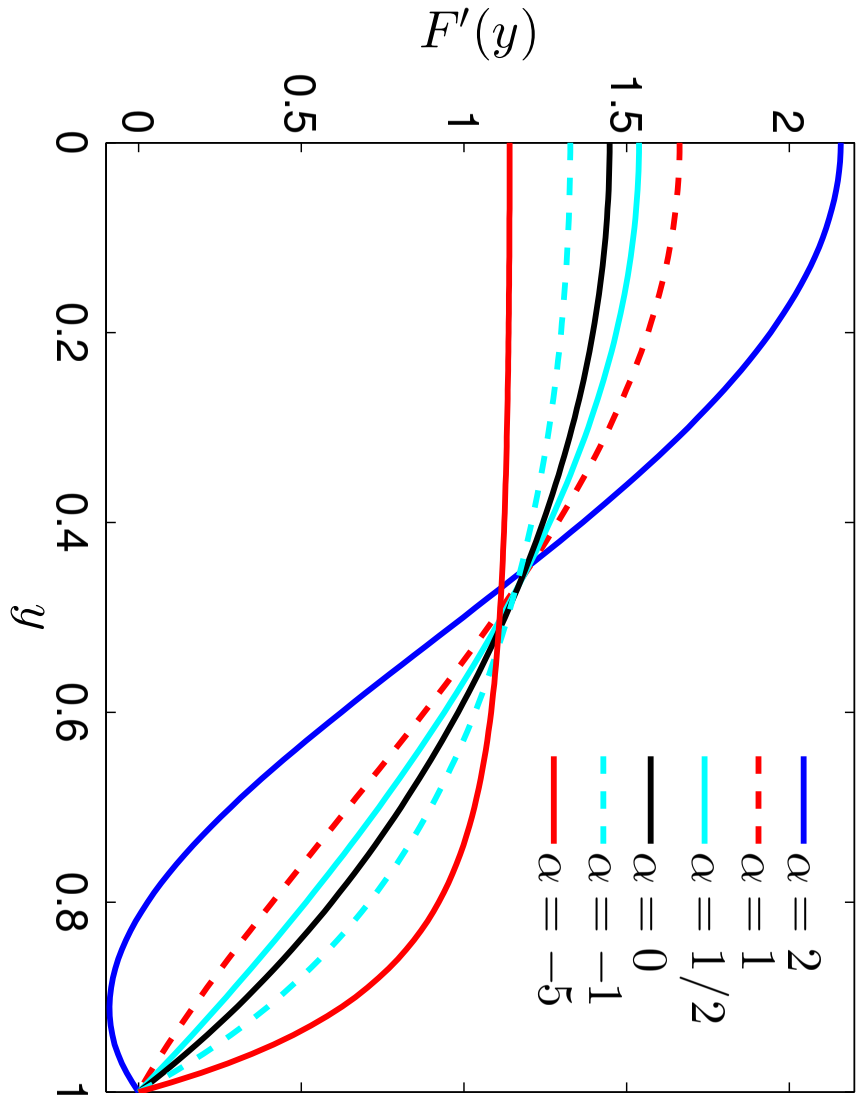

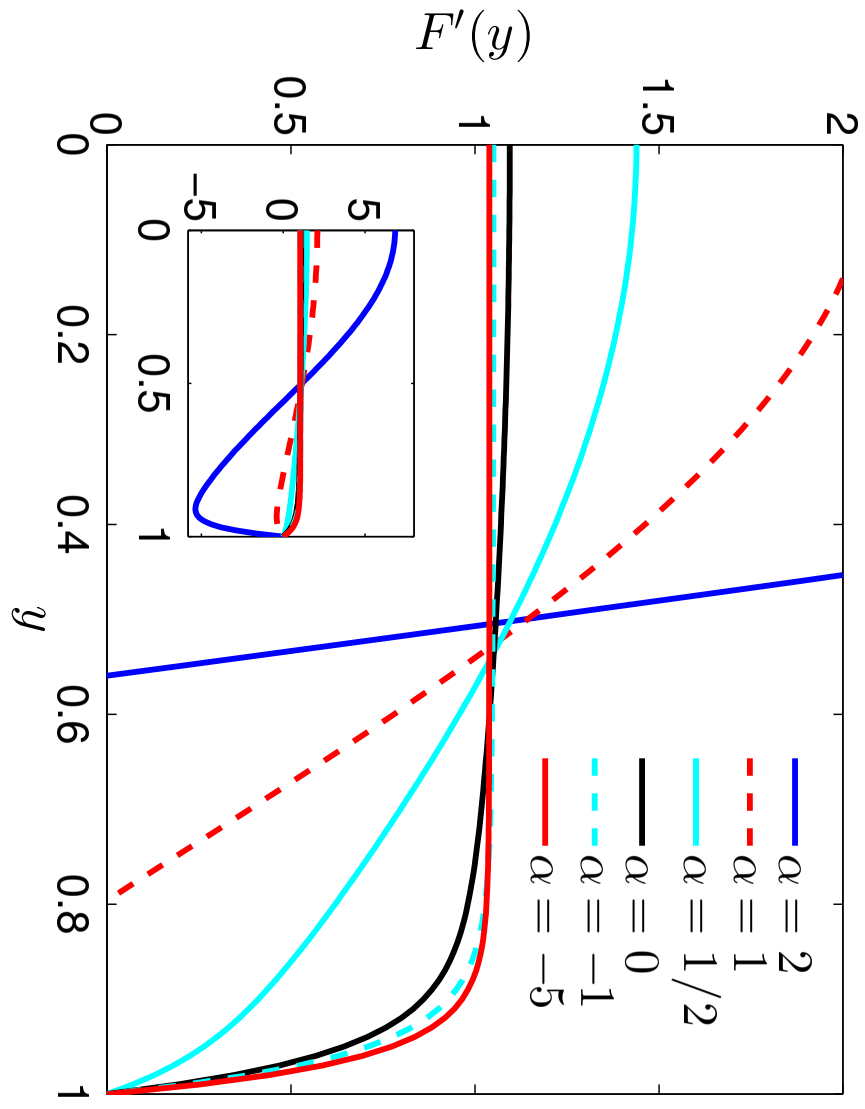

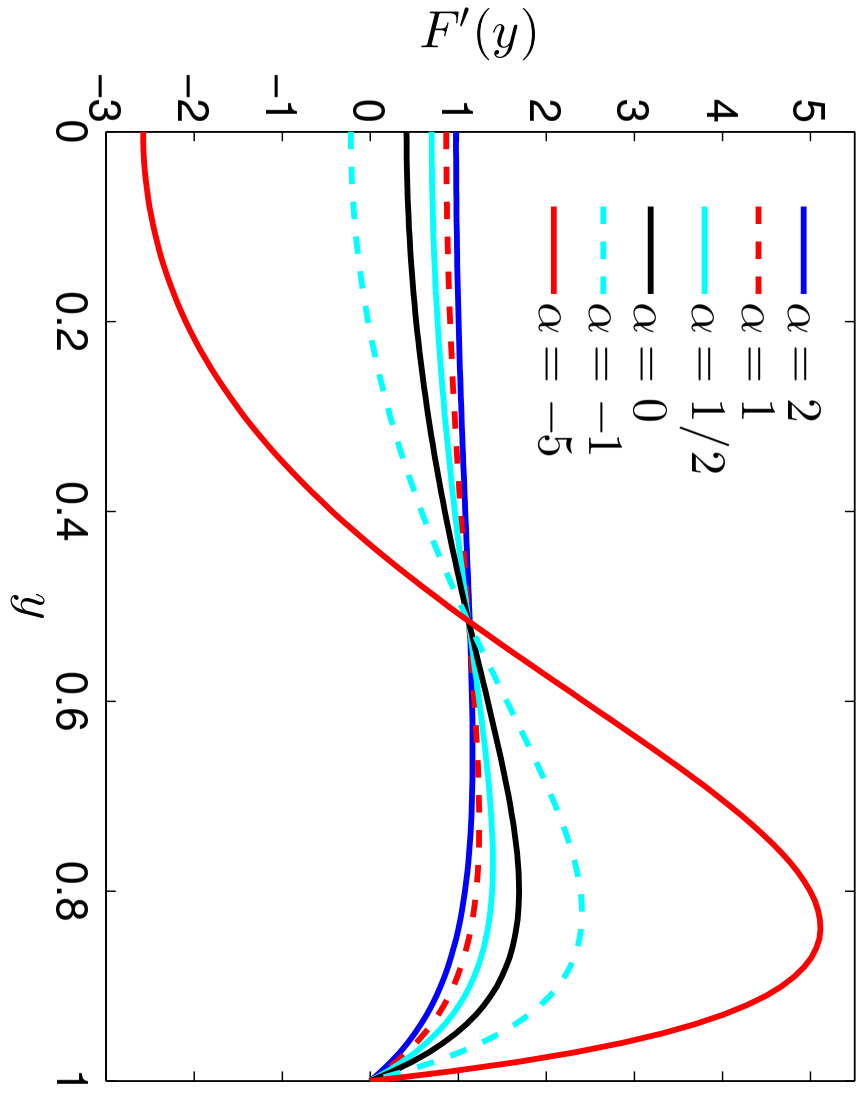

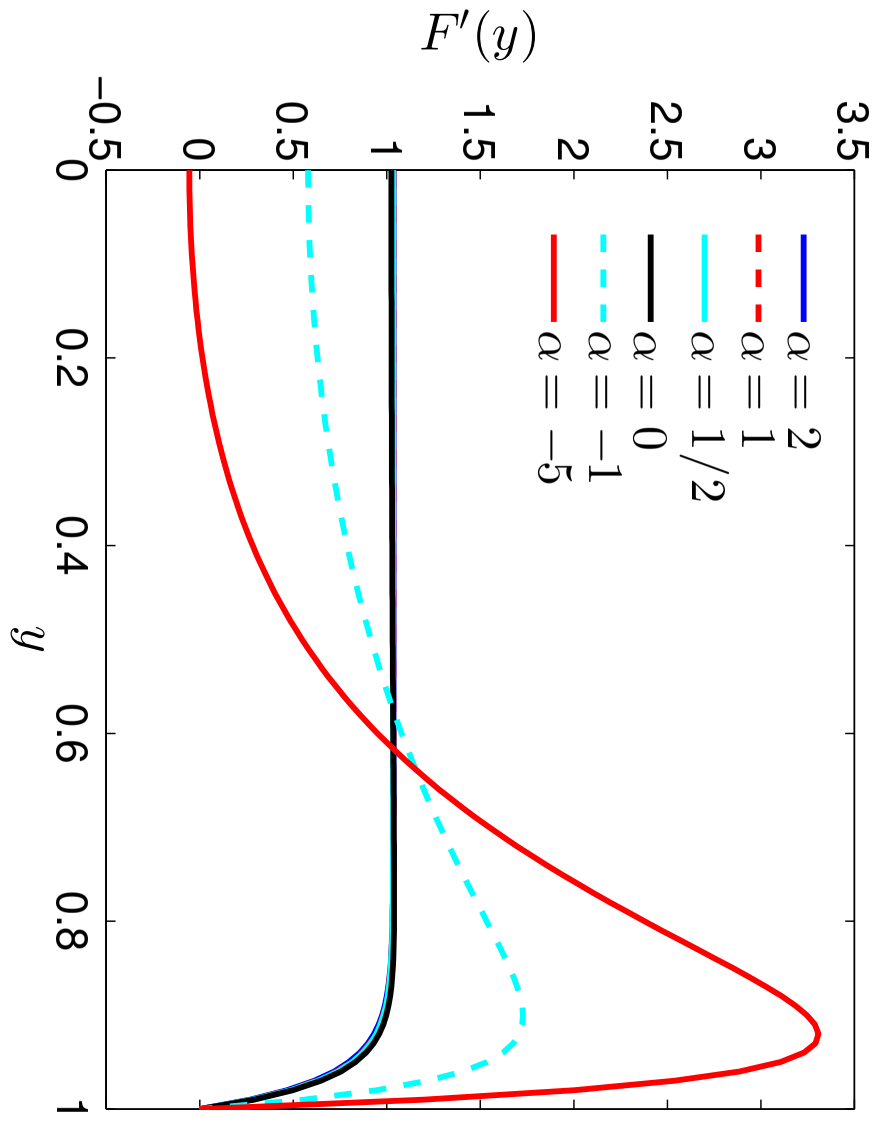

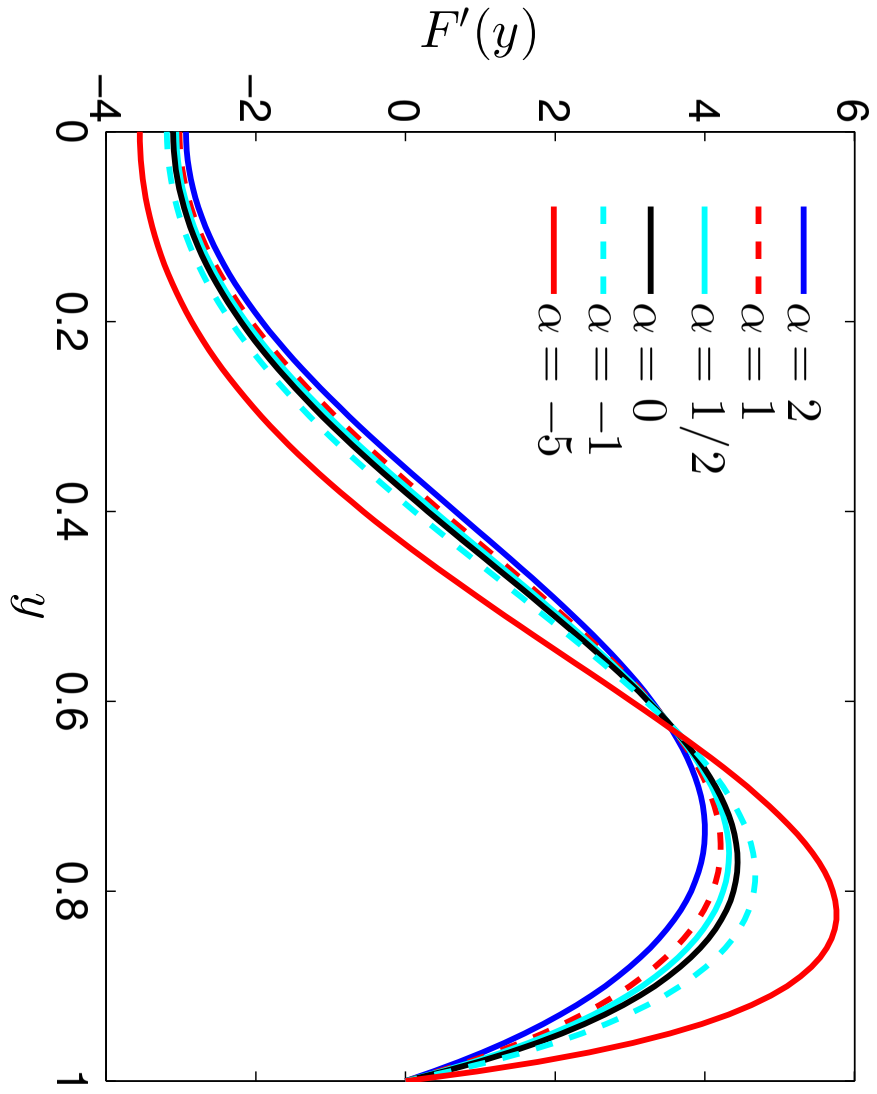

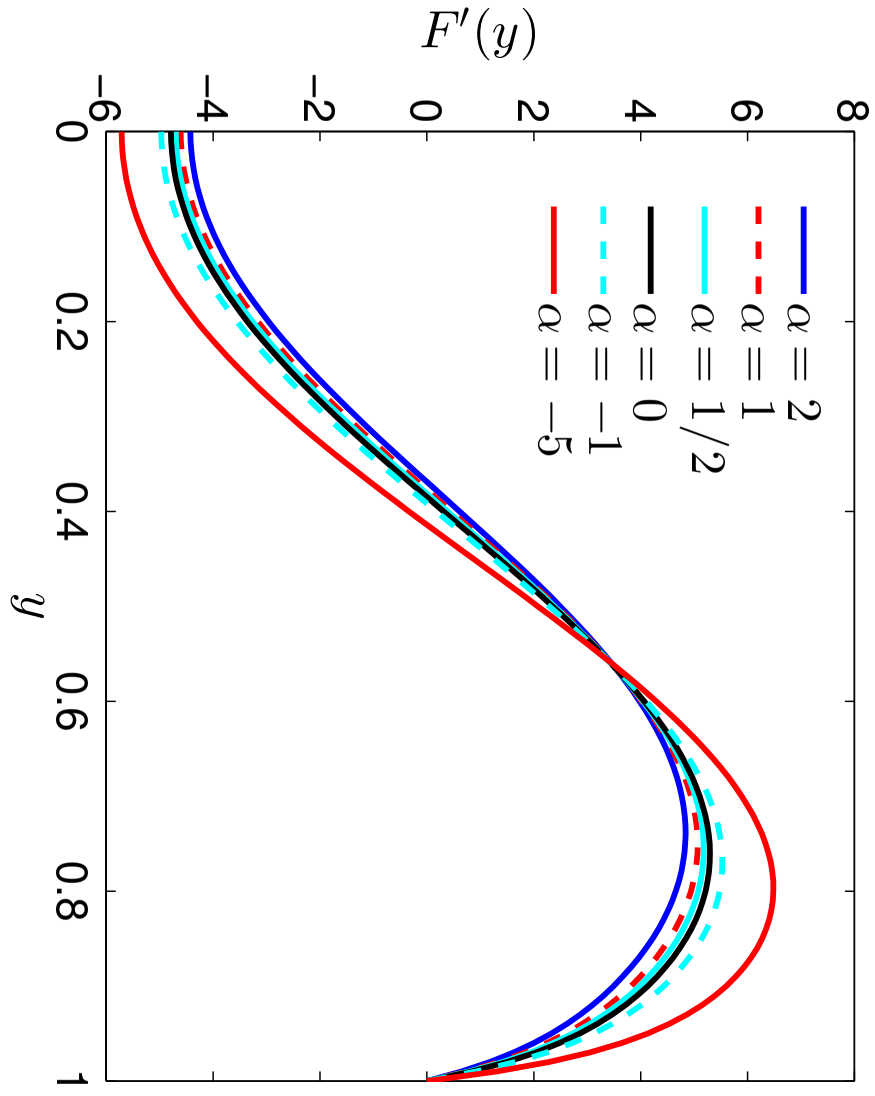

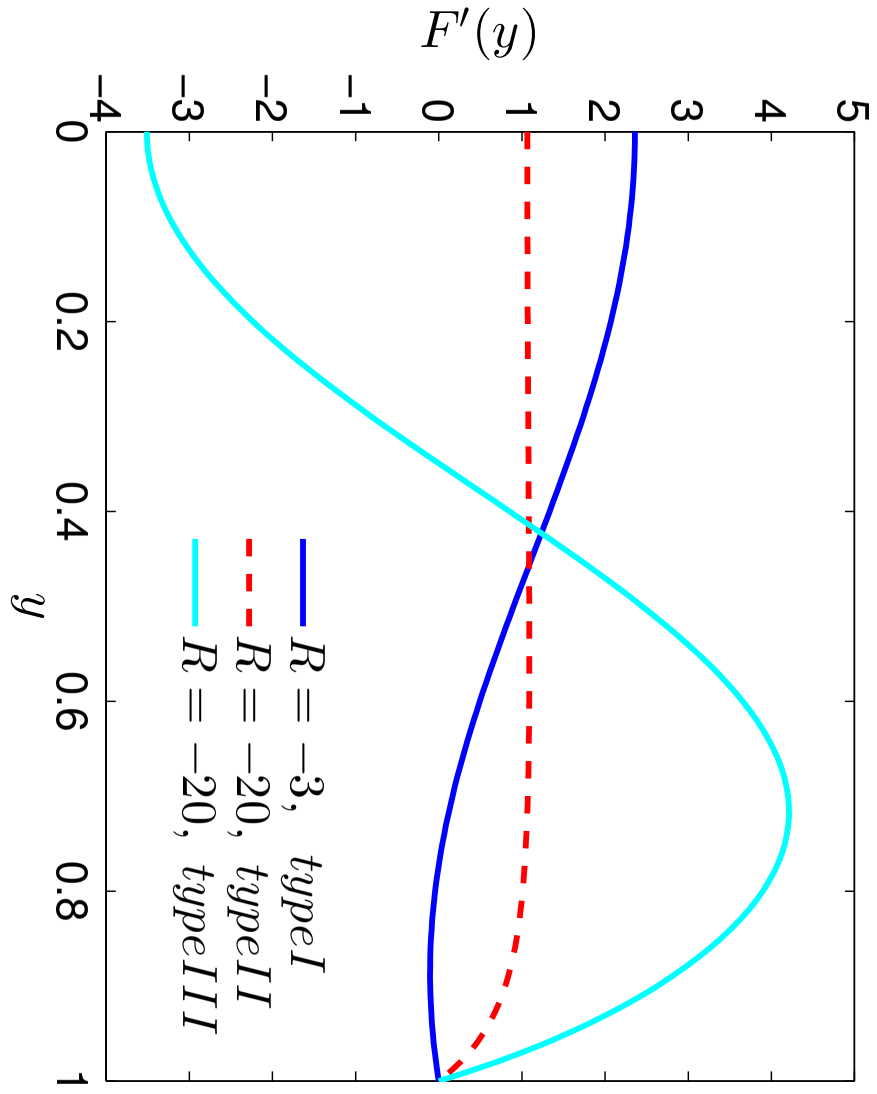

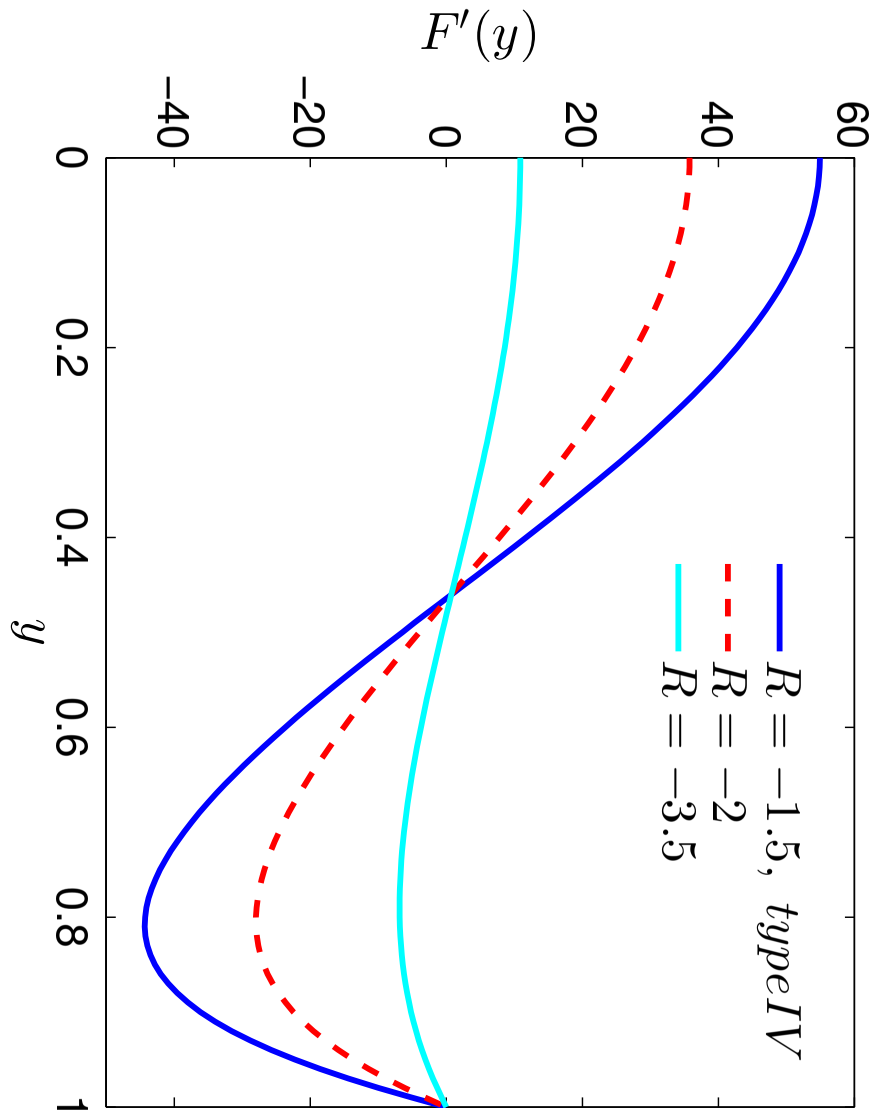

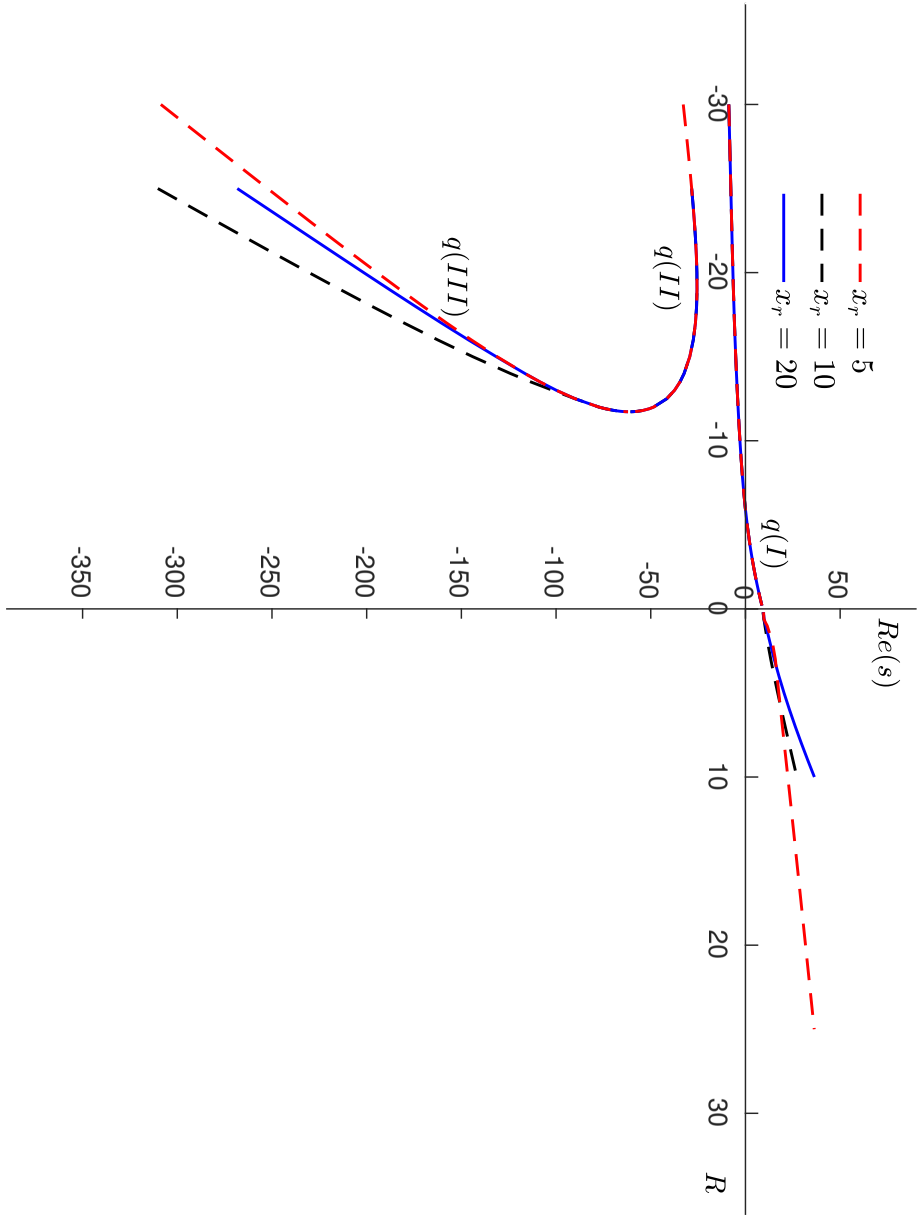

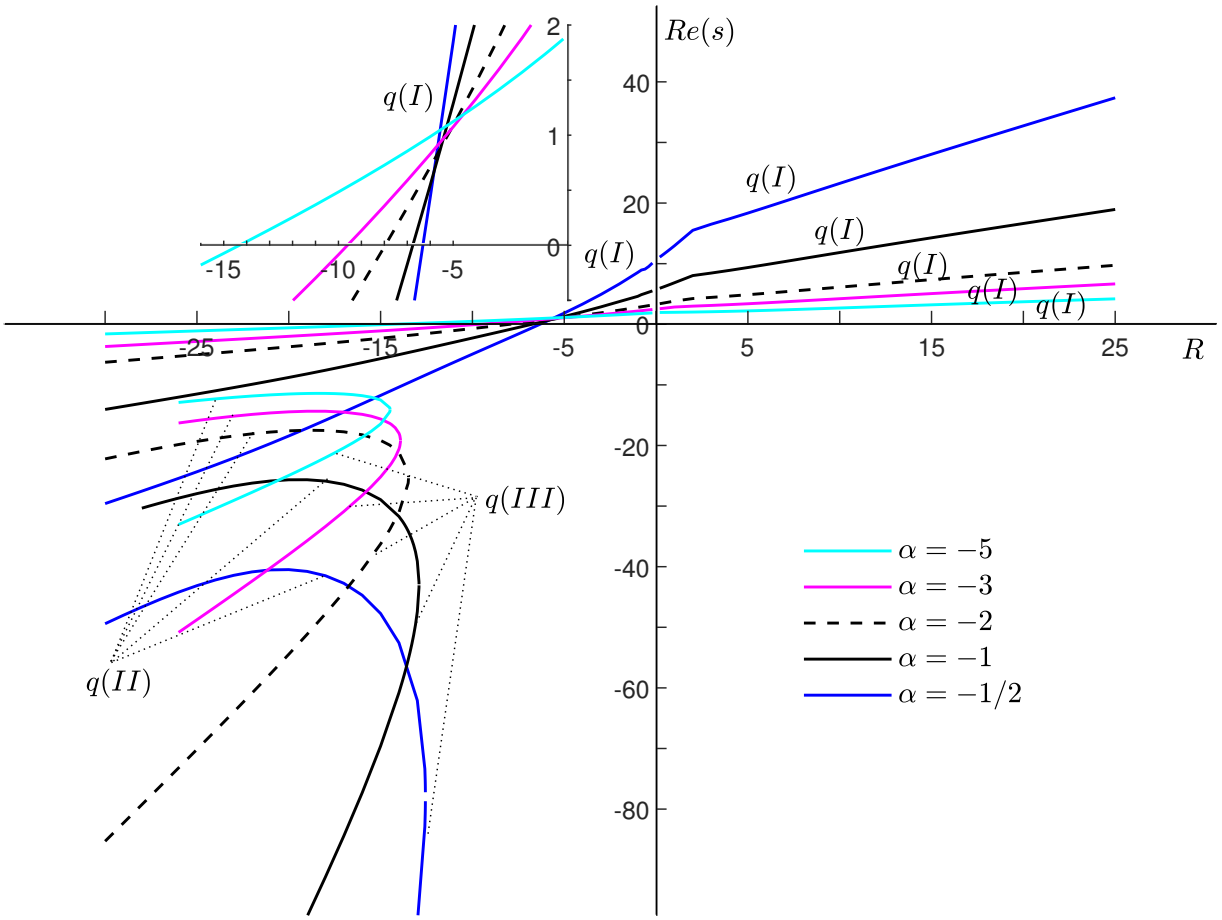

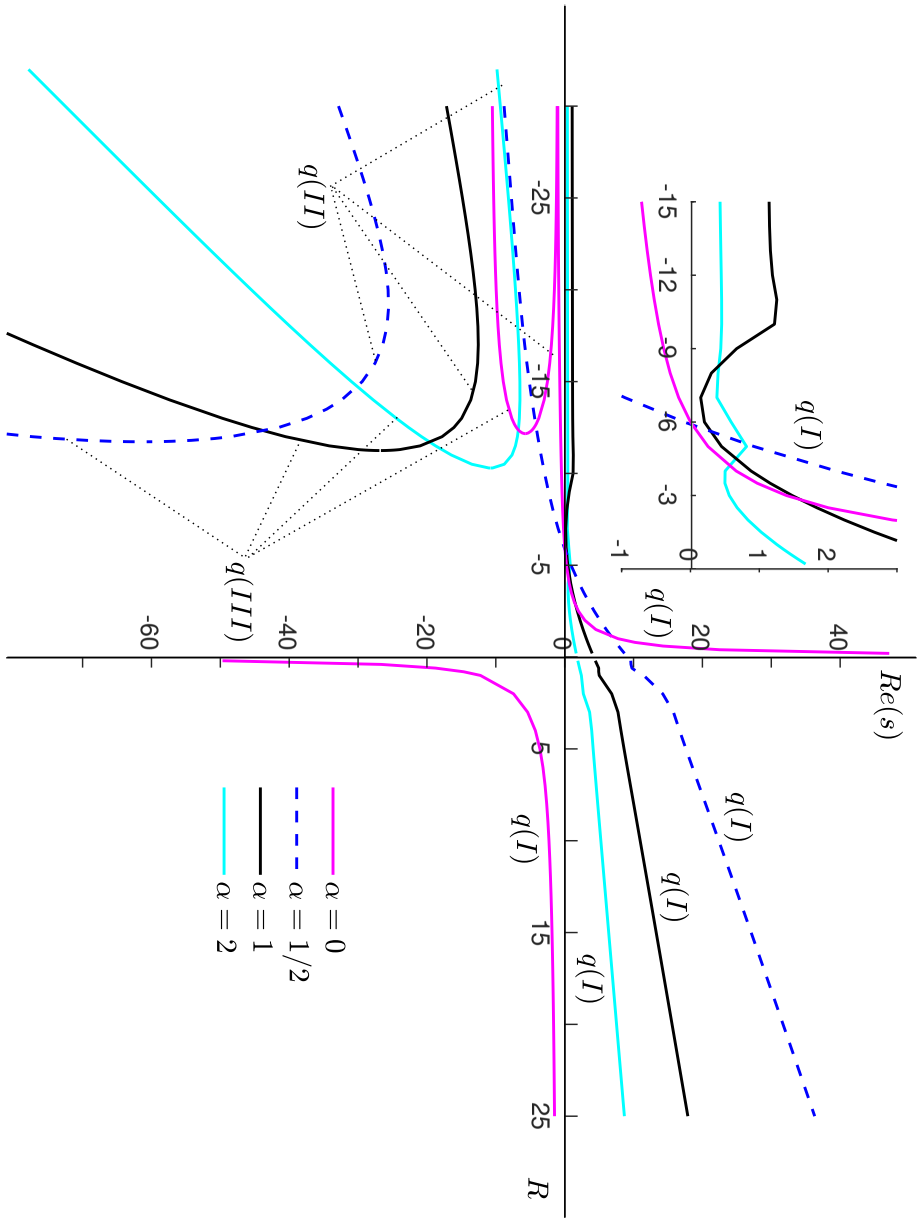

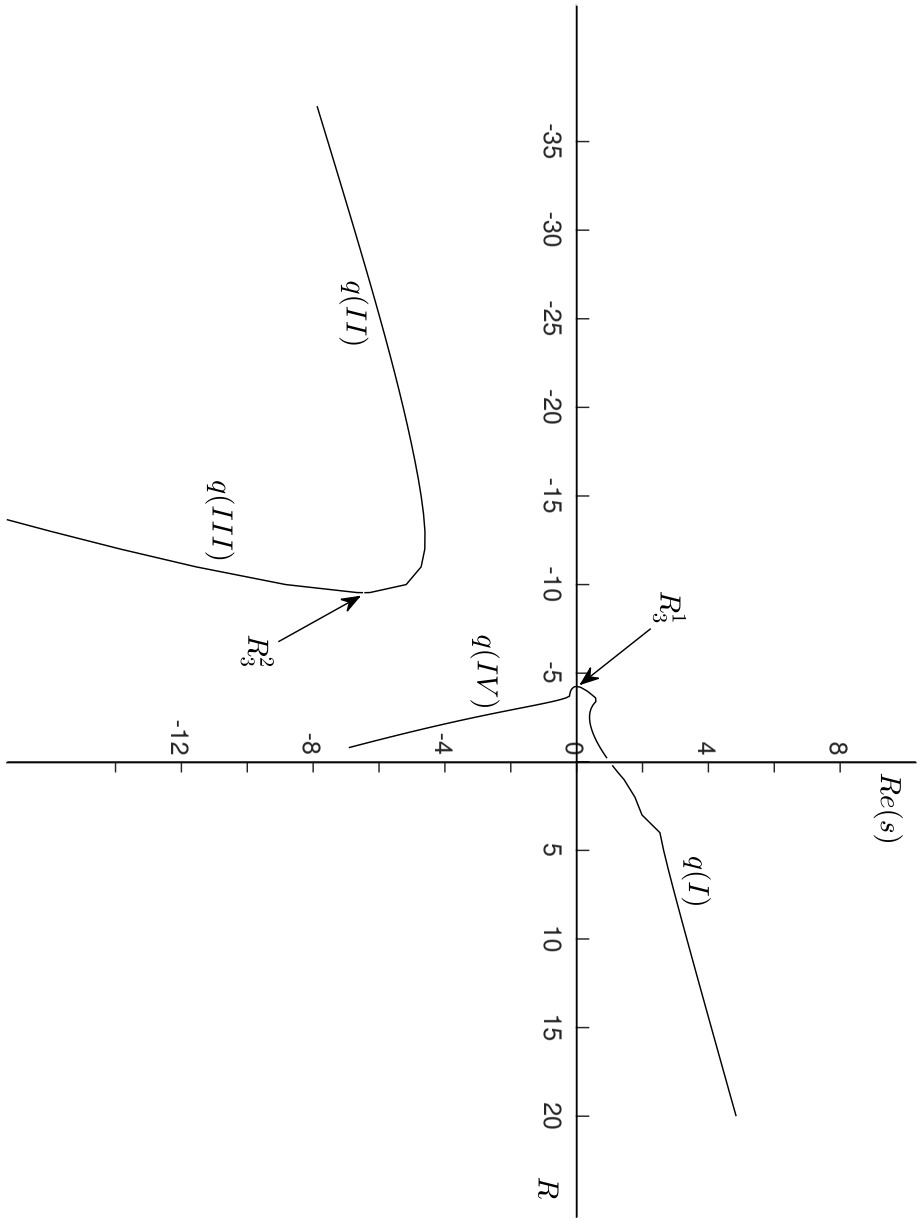

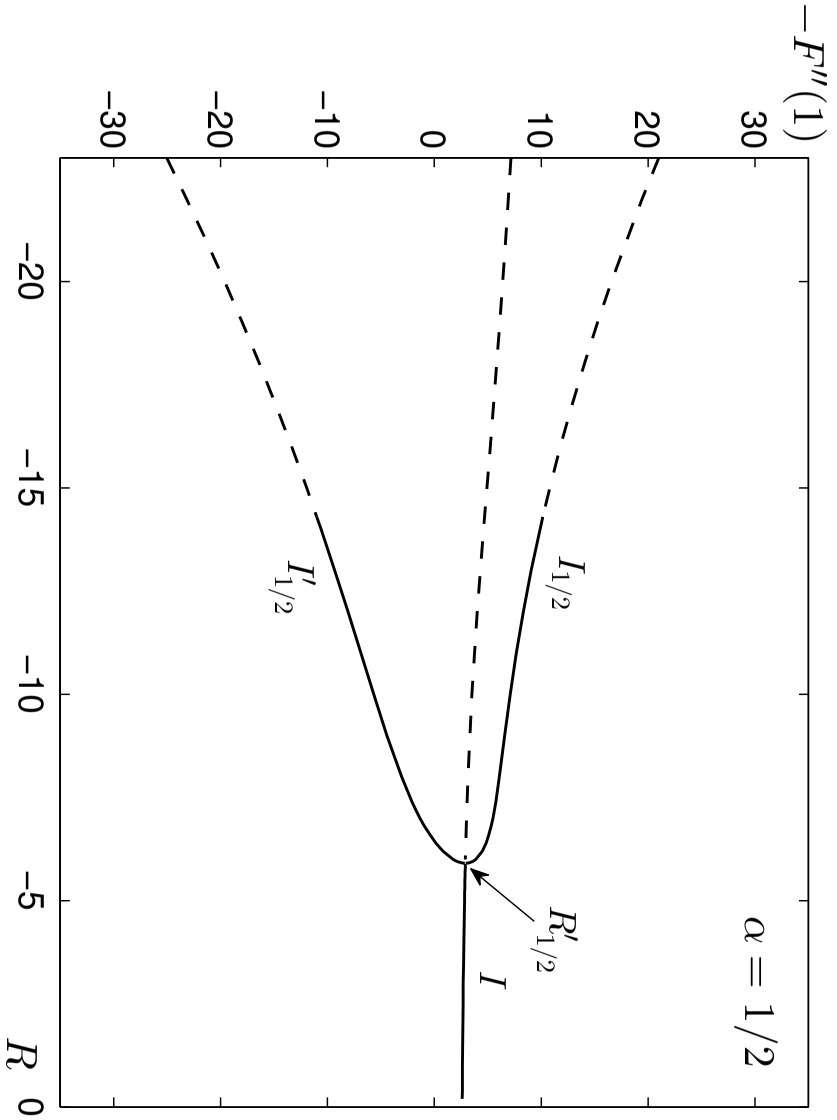

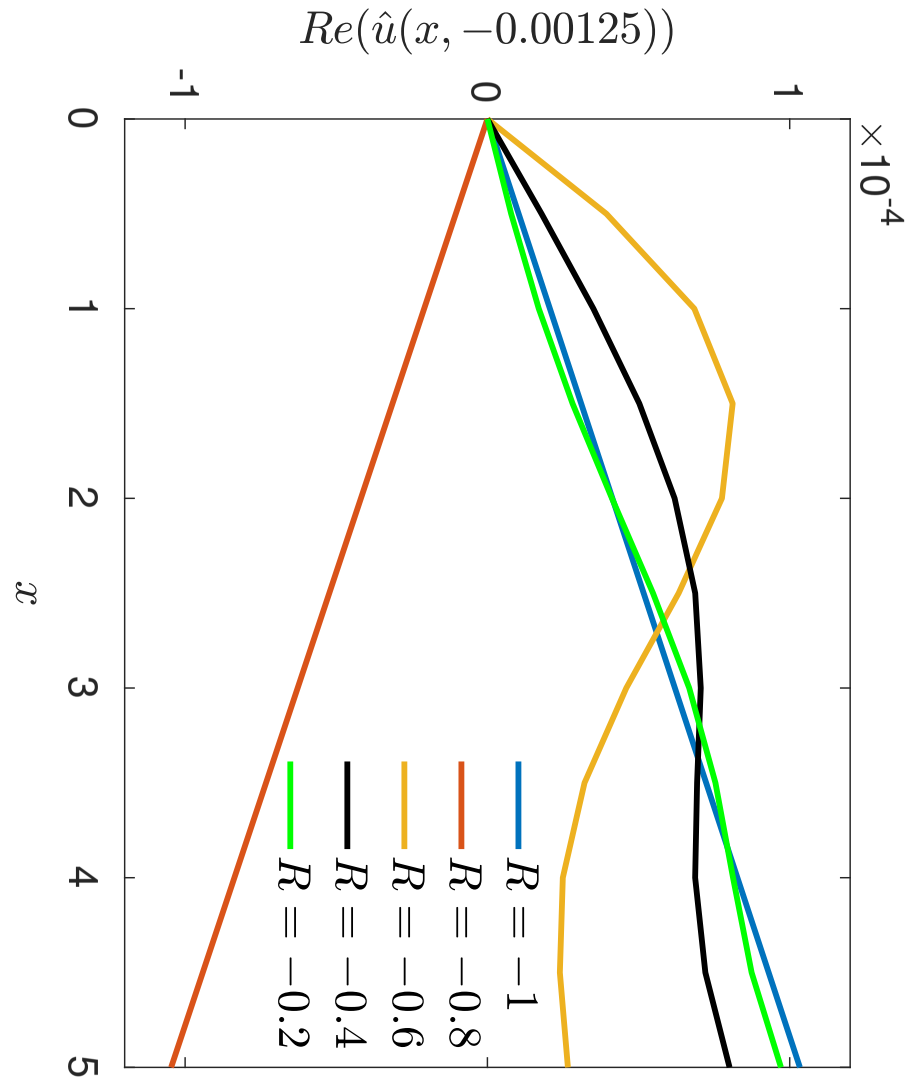

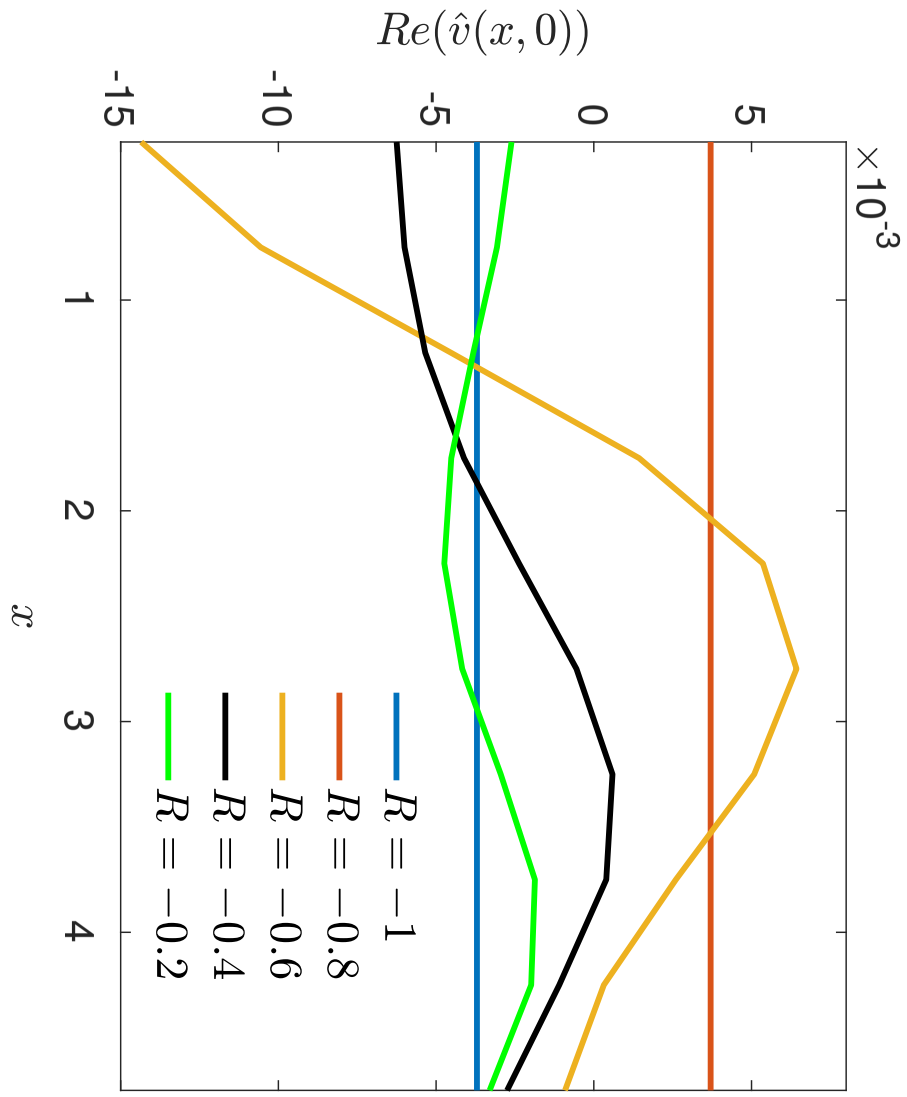

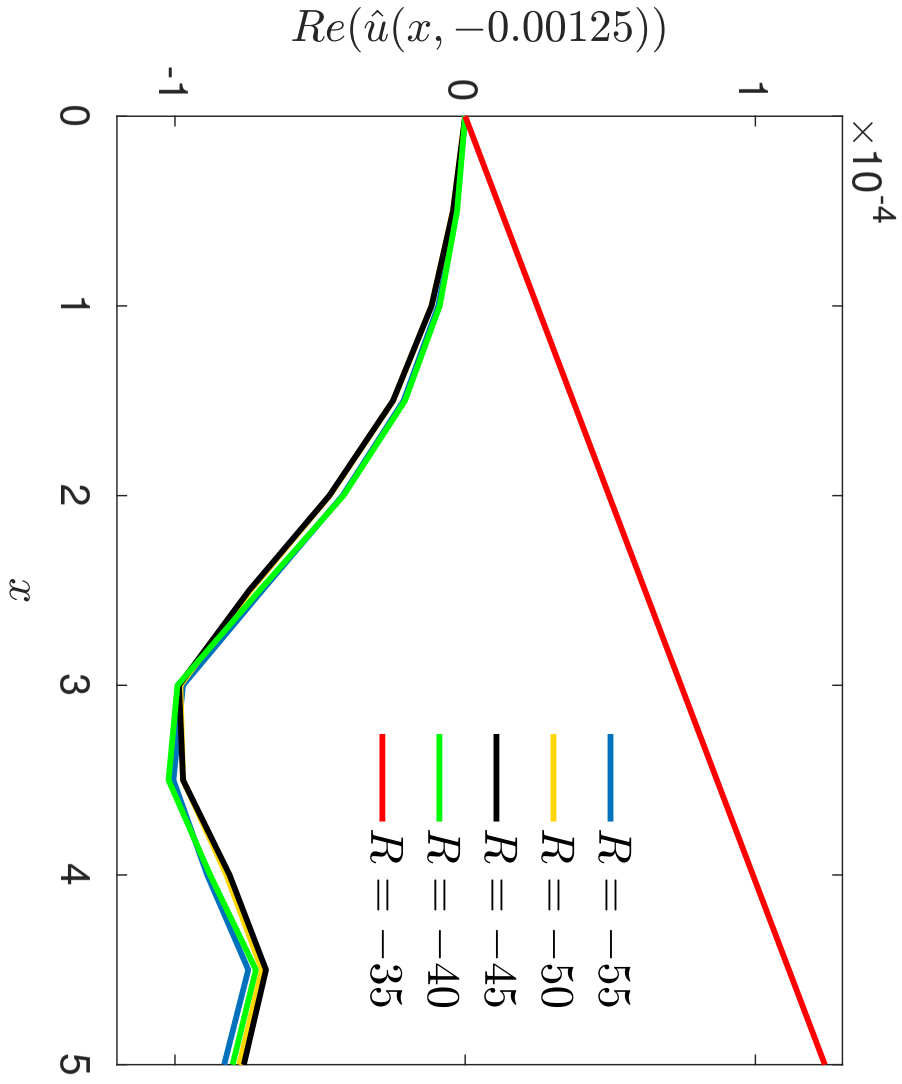

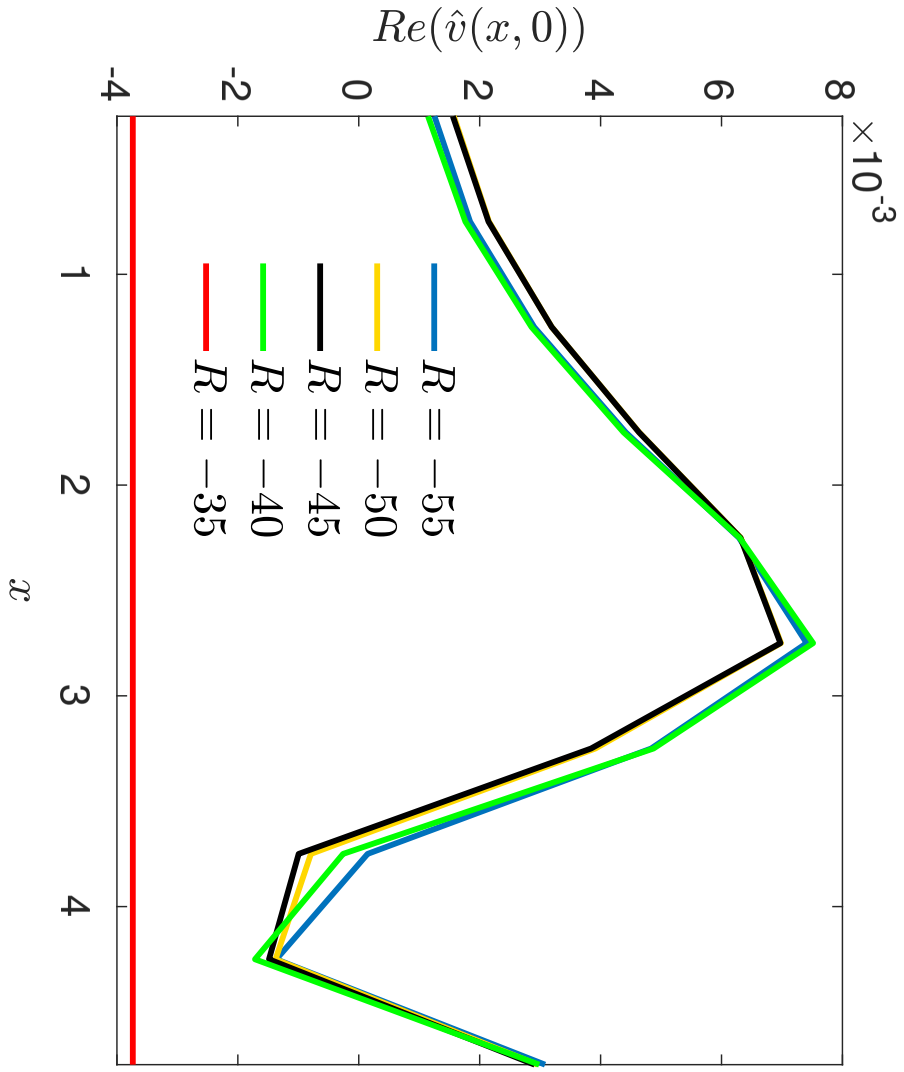

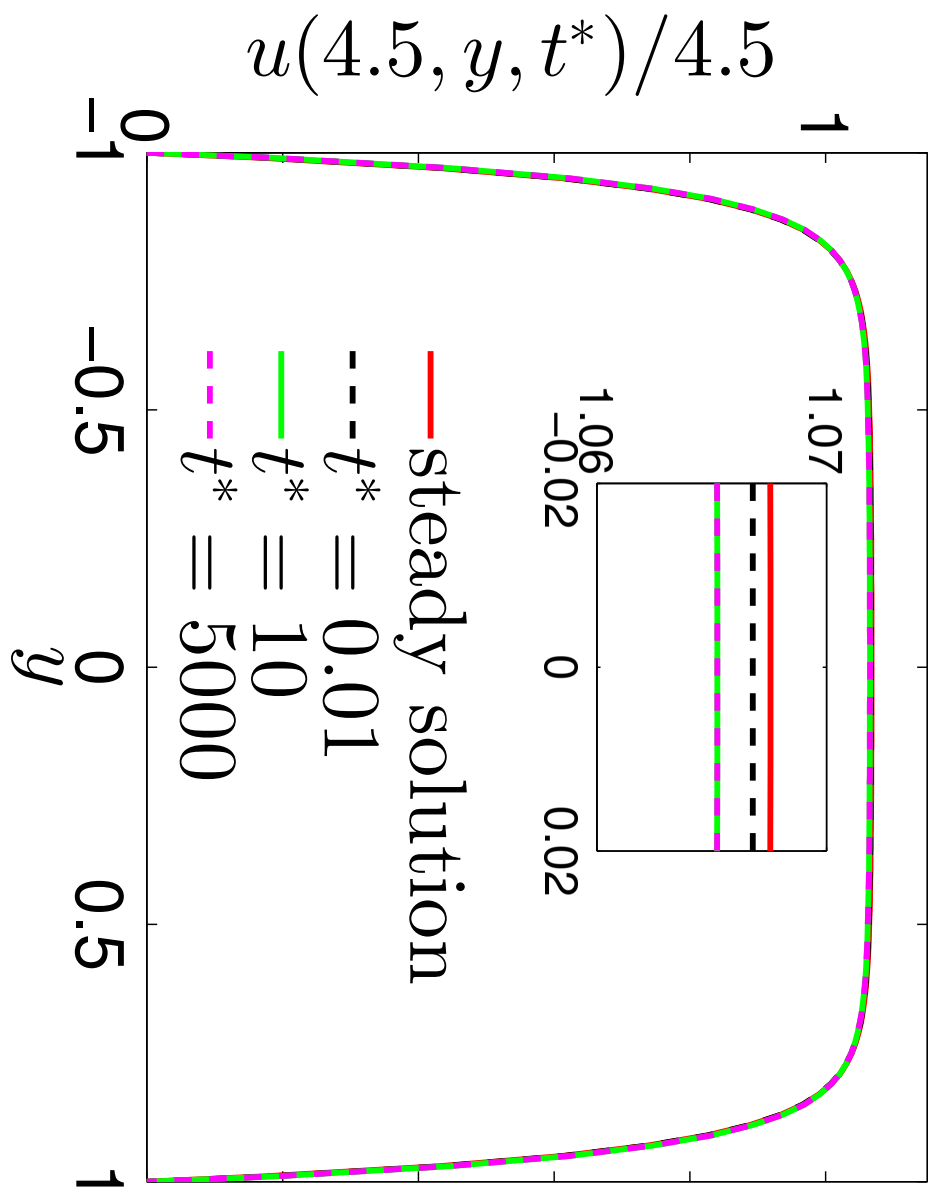

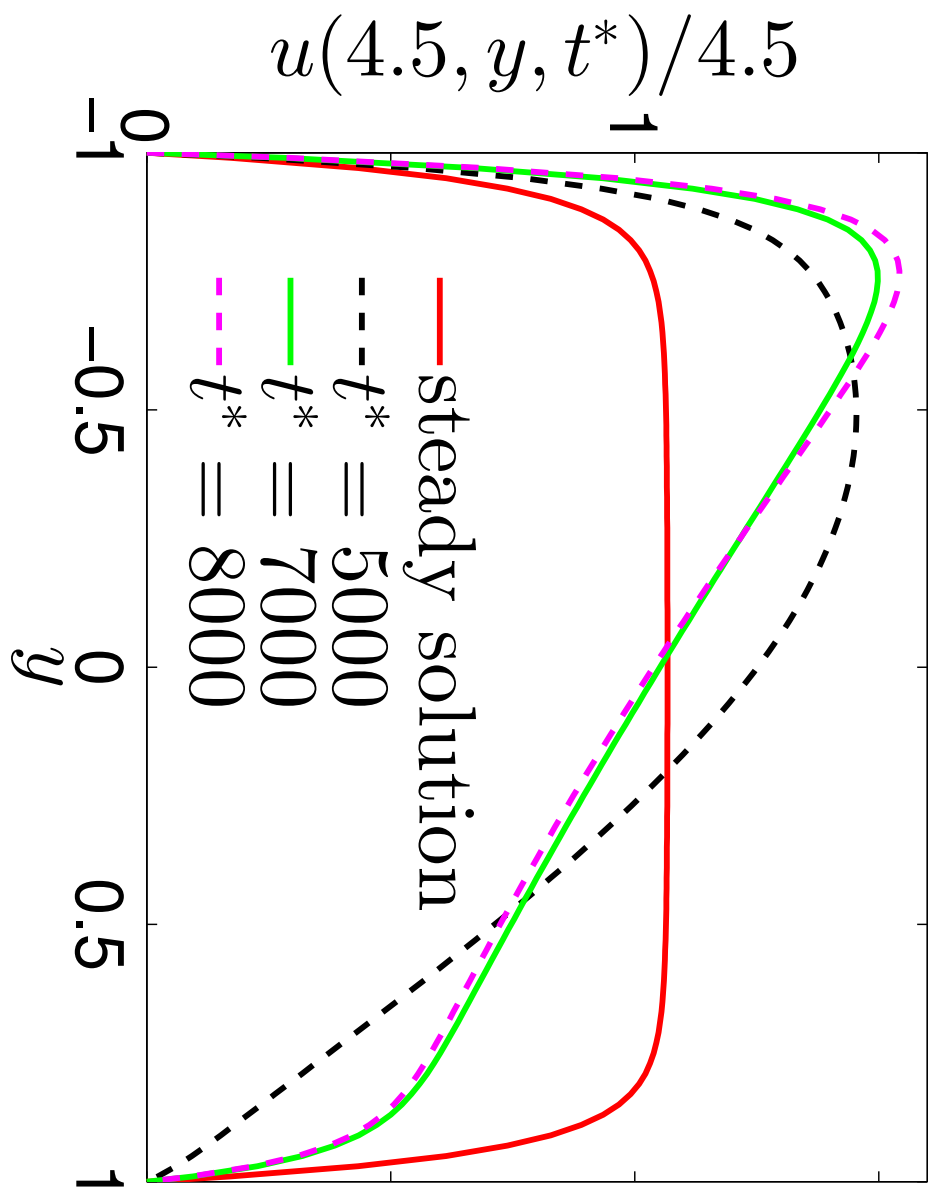

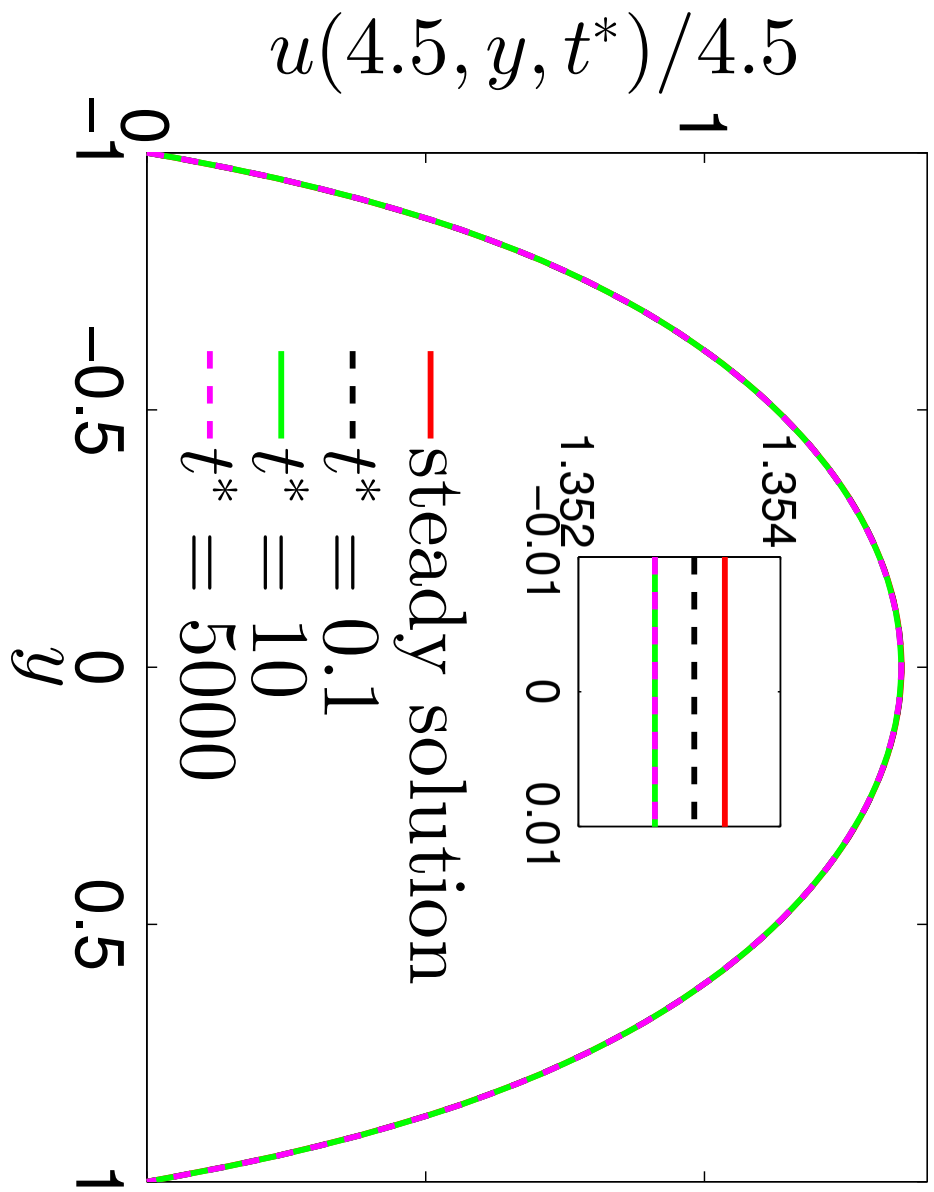

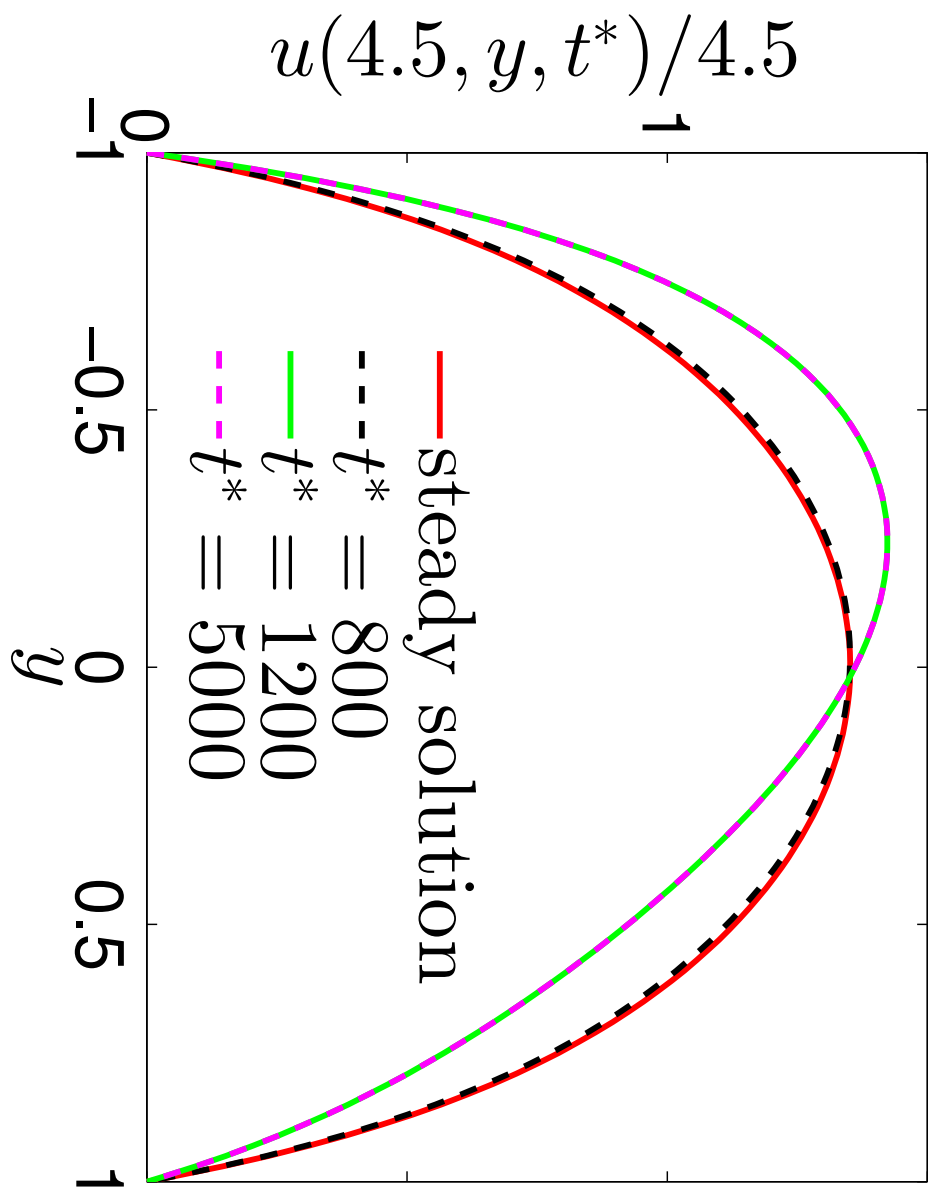

PLEASE CITE THIS ARTICLE AS DOI: 10.1063/5.0051846

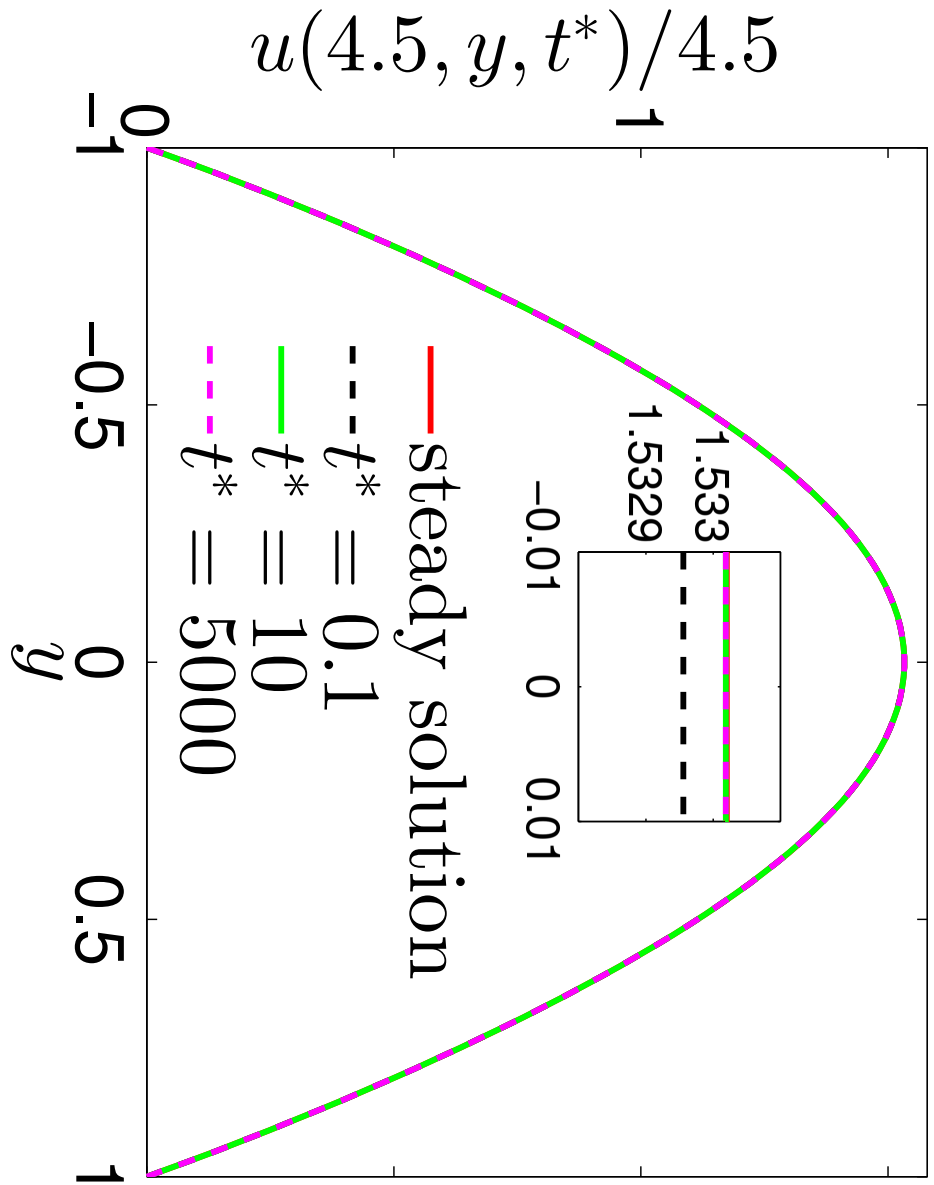

PLEASE CITE THIS ARTICLE AS DOI: 10.1063/5.0051846